The unexpectedly short Holocene Humid Period in Northern Arabia

Ina Neugebauer[1], Michèle Dinies[2], Birgit Plessen[1], Nadine Dräger[1], Achim Brauer[1], Helmut Brückner[3], Peter Frenzel[4], Gerd Gleixner[5], Philipp Hoelzmann[6], Kim J Krahn[7], Anna Pint[4], Valérie F Schwab[5], Anja Schwarz[7], Rik Tjallingii[1], and Max Engel[8]

[1]GFZ German Research Centre for Geosciences
[2]German Archaeological Institute (DAI)
[3]University of Cologne
[4]Friedrich Schiller University Jena
[5]Max Planck Institute for Biogeochemistry Jena
[6]Freie Universität Berlin
[7]Technische Universität Braunschweig
[8]Heidelberg University

November 23, 2022

Abstract

The early to middle Holocene Humid Period (HHP) was the last time when precession-forced intensification of summer monsoons and northward migration of associated rainfalls led to a greening of today's arid Saharo-Arabian desert belt. While this wet phase is well confined in N Africa and the S Arabian Peninsula, robust evidence from N Arabia is lacking. Here, we fill this gap with unprecedented annually to sub-decadally resolved proxy data from Tayma, the only known varved lake sediments in N Arabia. Based on stable isotopes, micro-facies analyses and precise varve and radiocarbon dating we distinguish five phases of lake development and prove that the wet phase in N Arabia from 8,800–7,900 years BP is considerably shorter than the commonly defined HHP (11,000–5,500 years BP). Moreover, we find a two century-long peak humidity at Tayma at times when a centennial-scale dry anomaly around 8,200 years BP interrupted the HHP in adjacent regions. This regional disparity is explained by an increased frequency of tropical plumes reaching N Arabia and compensating for the weakened monsoons and/or winter rains. This peak humidity possibly favoured Neolithic migrations into N Arabia indicating very dynamic human response to environmental changes.

Submitted to *Communications Earth & Environment*

The unexpectedly short Holocene Humid Period in Northern Arabia

Ina Neugebauer[1,2], Michèle Dinies[3,4], Birgit Plessen[1], Nadine Dräger[1], Achim Brauer[1], Helmut Brückner[5], Peter Frenzel[6], Gerd Gleixner[7], Philipp Hoelzmann[4], Kim J. Krahn[8], Anna Pint[6], Valérie F. Schwab[7], Anja Schwarz[8], Rik Tjallingii[1] and Max Engel[9,10,*]

1 GFZ German Research Centre for Geosciences, Section Climate Dynamics and Landscape Evolution, Telegrafenberg, 14473 Potsdam, Germany

2 University of Geneva, Department of Earth Sciences, Rue des Maraichers 13, 1205 Genève, Switzerland

3 German Archaeological Institute (DAI), Scientific Department of the Head Office, Im Dol 2–6, 14195 Berlin, Germany

4 Freie Universität Berlin, Institute of Geographical Sciences, Malteser Str. 74-100, 12249 Berlin, Germany

5 University of Cologne, Institute of Geography, Zülpicher Str. 45, 50674 Köln, Germany

6 Friedrich Schiller University Jena, Institute of Earth Sciences, Burgweg 11, 07749 Jena, Germany

7 Max Planck Institute for Biogeochemistry, Research Group Molecular Biogeochemistry, Hans-Knöll-Str. 10, 07745 Jena, Germany

8 Technische Universität Braunschweig, Institute of Geosystems and Bioindication, Langer Kamp 19c, 38106 Braunschweig, Germany

9 Heidelberg University, Institute of Geography, Im Neuenheimer Feld 348, 69120 Heidelberg, Germany

10 Royal Belgian Institute of Natural Sciences, Geological Survey of Belgium, Jennerstraat 13, 1000 Brussels, Belgium

* Corresponding author: Max Engel, max.engel@uni-heidelberg.de

Abstract

The early to middle Holocene Humid Period (HHP) was the last time when precession-forced intensification of summer monsoons and northward migration of associated rainfalls led to a greening of today's arid Saharo-Arabian desert belt. While this wet phase is well confined in N Africa and the S Arabian Peninsula, robust evidence from N Arabia is lacking. Here, we fill this gap with unprecedented annually to sub-decadally resolved proxy data from Tayma, the only known varved lake sediments in N Arabia. Based on stable isotopes, micro-facies analyses and precise varve and radiocarbon dating we distinguish five phases of lake development and prove that the wet phase in N Arabia from 8,800–7,900 years BP is considerably shorter than the commonly defined HHP (11,000–5,500 years BP). Moreover, we find a two century-long peak humidity at Tayma at times when a centennial-scale dry anomaly around 8,200 years BP interrupted the HHP in adjacent regions. This regional disparity is explained by an increased frequency of tropical plumes reaching N Arabia and compensating for the weakened monsoons and/or winter rains. This peak humidity possibly favoured Neolithic migrations into N Arabia indicating very dynamic human response to environmental changes.

Past millennial-scale pluvial periods are thought to have facilitated human dispersal out of Africa[1–3] by providing 'green corridors' through today's arid Saharo-Arabian desert belt[4–6]. Only recently, the Arabian Peninsula got into the focus of human-climate interaction studies, as it demonstrates high ecological sensitivity to climatic changes and represents the geographic nexus between Africa and Asia[1–3,7,8], while the role of the early to middle Holocene Humid Period (HHP) in Neolithic migrations and cultural progress has also been investigated[9,10]. The recent wave of research in Arabia has fundamentally transformed our perception of Arabian prehistory, including discoveries of Middle Palaeolithic (MIS 5 or even older) sites in Central Arabia[11] or traces of *Homo sapiens* in the Nefud desert at approx. 87 ka[8], *i.e.* phases associated with conditions more humid than today[2,6].

Climate models suggest that the N African monsoon was the dominant moisture source on the Arabian Peninsula during pluvials[1,12]. Yet, this remains a matter of debate for the N Arabian desert[13–15], as stronger insolation intensified and extended both African summer monsoons[1,2,12,16,17] and Mediterranean winter rains[3,18], the latter being the main source of moisture in this region today. In addition, tropical plumes (TPs), *i.e.* tropical synoptic disturbances conveying water vapour as continuous mid-upper tropospheric cloud bands from the Intertropical Convergence Zone (ITCZ) to >15°N, are known to affect N Arabia during winter and spring[14,19,20]. Higher frequency of such patterns during past pluvials was suggested to have contributed significant rainfall to the Saharo-Arabian desert[14,21,22], even though their past role as a moisture source remains poorly understood.

The rich archaeological heritage of Arabia is currently unravelled by major research initiatives[7,10,23] and "potentially thousands of water bodies" have been reconstructed for past pluvials[24], but it is still unknown how these water bodies and human habitats exactly looked like and for how long they existed[14,15]. Only a few climate records are available from speleothems in the wider region, i.e. the Levant[25–27] and S Arabia[28,29]. The entire lack of high-resolution palaeoclimate data from N Arabia leads to an inconsistent picture about the timing and magnitude of the HHP for this culturally important corridor to the Middle East, where some lower-resolution lacustrine records have pointed to more humid conditions during MIS 5 and the early to mid-Holocene[9,30–32].

The Tayma palaeolake record[4,33] is the only known high-resolution archive of the HHP in N Arabia providing insights into the early to mid-Holocene hydroclimate variability in unprecedented detail. Today, the 20 km^2-sized inland sabkha of Tayma with a 660 km^2

hydrological catchment (Fig. 1; Supplementary Figs. 1, 2), located at 27°40'N within the arid desert's interior, receives only scarce rains (on average 45 mm a^{-1}) from Mediterranean winter storms, occasional cross-Saharan tropical plumes or Red Sea cyclones between autumn and spring[14] (Fig. 1). Previous investigations of shoreline deposits (Supplementary Figs. 3–5) and sediment cores from the sabkha basin have proven the existence of a >17 m deep, perennial groundwater-supported lake[15] and the spread of grassland[4] during the early Holocene. The catchment-lake ratio (Fig. 1b; Supplementary Fig. 1b) and the short duration of the peak lake phase[4,15,33] exclude the influence of tectonics on lake-level changes, emphasising the significance of the lake as a palaeoclimate archive that is mainly controlled by rainfall and groundwater inflow. Yet, a precise determination of the lake phases was still missing, preventing a detailed view on the evolution of the palaeolake and the palaeoclimatological implications.

Chronology of the Tayma palaeolake record

The Tayma palaeolake record partly contains annually laminated sediments that were counted under the microscope (see Methods, Fig. 2, Supplementary Fig. 9). The new high-resolution age-depth model integrates AMS radiocarbon ages of pollen concentrates, microscopic varve counting and the independent age of a cryptotephra[34] in a Bayesian model (see Methods, Supplementary Table 1, Supplementary Fig. 7). The floating varve chronology comprising 650 ± 40 couplets is anchored to the radiocarbon age scale and constrains the varved lake phase at Tayma to 8,550–7,900 ± 40 cal varve yr BP (± 90 cal yr BP including the ^{14}C measurement error). A robust time marker is provided by the identification of the central Anatolian 'S1' tephra in the lower part of the record, dated in the Dead Sea record to 8,983 ± 83 cal yr BP[34]. The lacustrine and wetland sediments in the Tayma basin deposited from ca. 9,250 to ca. 4,200 cal yr BP (Supplement Fig. 7).

Groundwater vs. rainfall signal in the Tayma record

Compound-specific hydrogen isotope compositions of plant-wax n-alkanes (δD_{wax}), as well as pore-, rain- and groundwater isotopes ($\delta^{18}O_{water}$ and δD_{water}) trace variations in moisture supply and rainfall amount (Fig. 2, Methods and Supplementary Fig. 8). Stable oxygen and carbon isotope compositions of single primary aragonite laminae ($\delta^{18}O_{arag}$ and $\delta^{13}C_{arag}$) and of bulk carbonates ($\delta^{18}O_{carb}$ and $\delta^{13}C_{carb}$) indicate changing ground- and surface-water inflow, lake-water evaporation and the lake-internal productivity (Fig. 2). These data allow to develop a robust scenario for the evolution of the lake. The most striking finding were minimum δD_{wax} values of about -11‰ δD_p (precipitation) for the shallow lake or wetland phase and significantly lighter values down to -28‰ for the Tayma palaeolake, reflecting higher rainfall between 8,800 and 7,950 cal yr BP due to increased precipitation and a probable amount effect (Methods and Supplement Fig. 8).

Evolution of the Tayma palaeolake

The evolution of the lake can be separated into phases I–V, followed by phases VI (wetland) and VII (sabkha). A basal zone from 9,250–8,800 cal yr BP (lake phase I) represents a shallow lake initiated by increasing rainfall and recharge of the local Saq aquifer, when clastic sediments were deposited in a deflated endorheic basin from a prevailing desert environment[4]. Carbonates precipitated with very high $\delta^{18}O_{carb}$ values of around +11‰ and low $\delta^{13}C_{carb}$ values of around -8‰. At ca. 8,800 cal yr BP (lake phase II), a sharp decrease of $\delta^{18}O_{carb}$ to +8‰, increasing $\delta^{13}C_{carb}$ (Fig. 2) and the *in-situ* deposition of the brackish-water ostracod *Cyprideis torosa* (Fig. 2e) indicate reduced lake-water evaporation and the initial establishment of a shallow, but perennial and increasingly productive water body[35] as a response to wetter conditions. At ca. 8,550 cal yr BP the formation of varves started (Fig. 2; Supplementary Figs. 6, 9), reflecting the onset of a deep (>17 m[15], Supplementary Figs. 3–5) and stratified lake that persisted for a period of 650 ± 40 varve years (lake phases III and IV).

From ca. 8,550 to 8,250 cal yr BP (lake phase III), variable but continuously decreasing plant wax $\delta D_{nC29,\ nC31}$ values between -100 and -150‰ indicate a humid period with enhanced seasonality[36,37]. The alternating deposition of dark clay- and organic-rich laminae and white, primary aragonite laminae reflects pronounced wet and dry seasons. The $\delta^{18}O_{carb/arag}$ values generally decrease from +8‰ to +6‰ simultaneously with progressively increasing $\delta^{13}C_{carb}$ values from about -6 up to +2‰ towards enhanced lake productivity. The positive excursion of $\delta^{18}O_{carb}$ to >+10‰ centred at ca. 8,400 cal yr BP reflects a decadal- to centennial-scale drawback to even stronger dry-season evaporation, which was compensated by enhanced humidity during the rainy season and groundwater inflow, sufficient to sustain a high lake level and varve formation.

From ca. 8,250 to 8,000 cal yr BP (lake phase IV) the highest production rate of organic matter in the lake, annual blooms of planktonic diatoms (mainly *Cyclotella* cf. *choctawhatcheeana*) (Supplementary Figs. 6, 9), greatest abundances of foraminifera, the lowest $\delta D_{nC29,\ nC31}$ values down to -155‰ and weakest dry-season evaporation with lowest $\delta^{18}O_{arag}$ values of +4‰ characterize the highest lake stand and most humid period at Tayma during the Holocene. This is supported by the distinct change in varve composition from evaporation-driven aragonite varves to productivity-fuelled diatom-aragonite varves and total organic carbon (TOC) contents of up to 5%. From about 8,200 cal yr BP the $\delta D_{nC29,\ nC31}$ values again start to vary between -140‰ and -100‰, and the $\delta^{18}O_{carb/arag}$ values increase from +4 to +8‰ (Fig. 2e; Supplementary Fig. 6).

At ca. 7,950 cal yr BP, ceasing diatom and aragonite laminae and more abundant clastic quartz grains of aeolian origin, as well as the first appearance of gypsum show a rapidly declining lake level (lake phase V). This led to the disappearance of varves within a few decades accompanied by a sharp reduction in TOC content and a decline of $\delta^{13}C_{carb}$ back to a level comparable to the early shallow-lake phase II, prior to 8,550 cal yr BP. Progressively enriched δD_{wax} values of up to -60‰ and $\delta^{18}O_{carb}$ values towards +12‰ reflect a significant decrease in surface- and groundwater inflow and a strongly increasing evaporation, indicating a gradual end of the humid phase over 100–150 years until ca. 7,800 cal yr BP.

Increasing gypsum precipitation and $\delta^{18}O_{carb}$ rising to +12‰ point to a shrinking lake under an increasingly arid climate between 7,800 and ca. 6,800 cal yr BP, after which wetland conditions set in with TOC levels close to 0 and further increasing aeolian influx (phase VI). Around ca. 4,200 cal yr BP greyish mud is replaced by reddish brown clastics mixed with gypsum (phase VII) (Supplementary Figs. 6, 7), reflecting a further aridisation pulse correlating with a dry event recorded at several sites in the E Mediterranean/Middle East, *e.g.* the N Red Sea[38].

Discussion

Our data support existing low-resolution N Arabian palaeoenvironmental records[9,10,30] but we prove that the HHP in N Arabia was remarkably short, lasting only ca. 650 years from 8,550 to 7,900 cal yr BP. In addition, we observe an intriguing regional hydroclimatic diversity, since the aforementioned peak humidity in N Arabia from 8,550 to 7,900 cal yr BP coincides with a widespread, centennial-scale dry anomaly centred around the 8.2 ka cold event at other low-latitude sites in the N Hemisphere such as the E Mediterranean or S Arabia[39] (Fig. 3). A low-latitude dry period between ca. 8,500 and 7,800 cal yr BP was the most pronounced hydroclimatic drawback of the HHP, evidenced *e.g.* in the desiccation or distinct lowstands of N African lakes[40] and diminished runoff of the Nile River[41], leading to re-oxygenation of the E Mediterranean Sea[42,43] (Fig. 3). Drought conditions mostly resulted from reduced summer-monsoon rainfall[28,29]. However, speleothem records from the Levantine region[25] and marine records from the E Mediterranean suggest that Mediterranean winter rains were reduced as well, as a result of temporary, meltwater-related deceleration of the North Atlantic thermohaline circulation[39,44] (Fig. 3).

We propose that synoptic-scale patterns, which are scarce today, played a more dominant role in delivering moisture to N Arabia between 8,250 and 8,000 cal yr BP resulting in a humidity peak in this region. We suggest that in particular more frequent tropical plumes (TP) led to a moisture surplus in N Arabia that compensated the reduced monsoonal and Mediterranean winter rains during the centennial dry anomaly related to the 8.2 ka event. In contrast to short and localised convective cells of the Active Red Sea Trough pattern (ARST) triggering flash floods in the southern Levant, TPs promote long-lasting moderate rains and thus more effective moisture over a larger region[19]. We presume that TP formation was favoured by ocean-atmosphere feedbacks during the 'cool poles – dry tropics' anomaly around 8.2 ka: lower sea-surface temperatures in the N Atlantic and Mediterranean Sea promote deeper, southwards penetrating mid-latitude troughs and stronger sub-tropical anticyclones (*i.e.* drier air masses). This leads to an intensification of tropical moisture advection and the sub-tropical jet stream, inducing jet streaks that reach as far as northern tropical W Africa and convey moist air to N Arabia at mid- to upper tropospheric levels[20]. The observed moisture surplus in combination with charged aquifers had distinct short-term impacts on the local environment and probably also on human migration. Vegetation resources[4] and the abundance of prey animals[12] increased and stimulated Neolithic migrations into N Arabia as evidenced by abundant Levant-type Pre-Pottery Neolithic A and B assemblages identified in the N branch of the Nefud desert[9,10].

Acknowledgements

This study is a contribution to the interdisciplinary research project "CLEAR – Holocene CLimatic Events of Northern ARabia" (https://clear2018.wordpress.com/), funded by Deutsche Forschungsgemeinschaft (DFG grants EN977/2-1, PL535/2-1, FR1489/5-1). The CLEAR project was kindly invited and supported by the Saudi-German Joint Archaeological Project at Tayma, led by Ricardo Eichmann, Arnulf Hausleiter (German Archaeological Institute) and Mohammed H. al-Najem (Museum of Archaeology and Ethnography, Tayma). We are grateful for the research permit issued by the Saudi Commission for Tourism and National Heritage, represented by HRH Prince Sultan bin Salman bin Abdulaziz al-Sa‘ud. Further support by Jenny Friedrich (sample preparation), Doreen Noack, Andrea Vieth-Hillebrand (GFZ) (hydrogen isotope measurements), Dieter Berger (GFZ) (preparation of thin sections), Christin Kramer (documentation) and Kirstin Jacobson (language editing) is greatly appreciated.

Author contributions

B.P., I.N., M.E. and P.F. designed the study. M.E., H.B., M.D. and A.P. collected the sediment cores. M.D. and I.N. constructed the age model. I.N., B.P., R.T., P.H. and A.B. contributed the sedimentological and microfacies data. B.P and I.N. contributed stable-isotope data on water and carbonates. N.D., V.F.S. and G.G. contributed the leaf-wax n-alkane data. A.P. and P.F. contributed foraminiferal and ostracod analyses. A.S. and K.J.K. contributed the diatom analysis. I.N., M.E. and B.P. wrote the manuscript. All authors discussed and commented on the manuscript.

Additional information

Data reported here are stored at GFZ Data Services (https://...). Supplementary information is available in the online version of the paper. Reprints and permissions information is available online at www.nature.com/reprints. Correspondence and requests for materials should be addressed to M.E.

Competing interests

The authors declare no competing financial or non-financial interests.

Figure legends

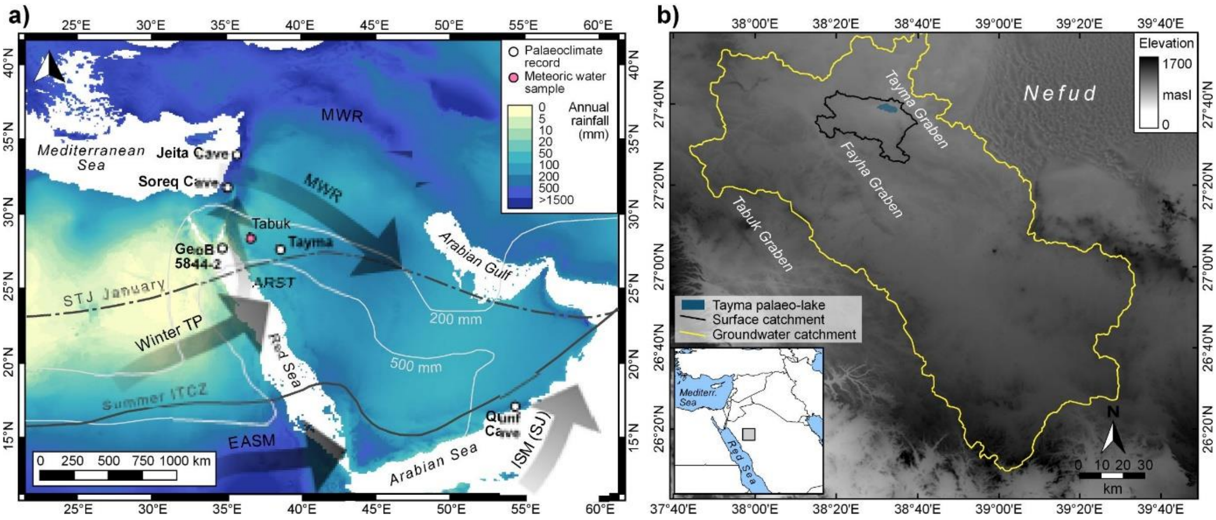

Figure 1: Regional context of Tayma. a) Overview of the Arabian Peninsula and adjacent areas with the key palaeoclimate sites of Jeita Cave[27], Soreq Cave[25,26], GeoB 5844-2 in the Red Sea[13] and Qunf Cave[28], mean annual rainfall 1970–2000 (WorldClim 2 dataset[45]), average positions of the Intertropical Convergence Zone (ITCZ) in summer and the Subtropical Jet (STJ) in winter[46], and atmospheric sources of regional precipitation (MWR = Mediterranean winter rains; Winter TP = Winter tropical plumes; EASM = East African Summer Monsoon; ISM (SJ) = Indian Summer Monsoon (SJ = Somali Jet); ARST = Active Red Sea Trough)[14]. b) Reconstructed extent during the peak phase of the Tayma palaeolake, today's surface catchment and groundwater catchment[47]. The topography is based on GTOPO30 data[48].

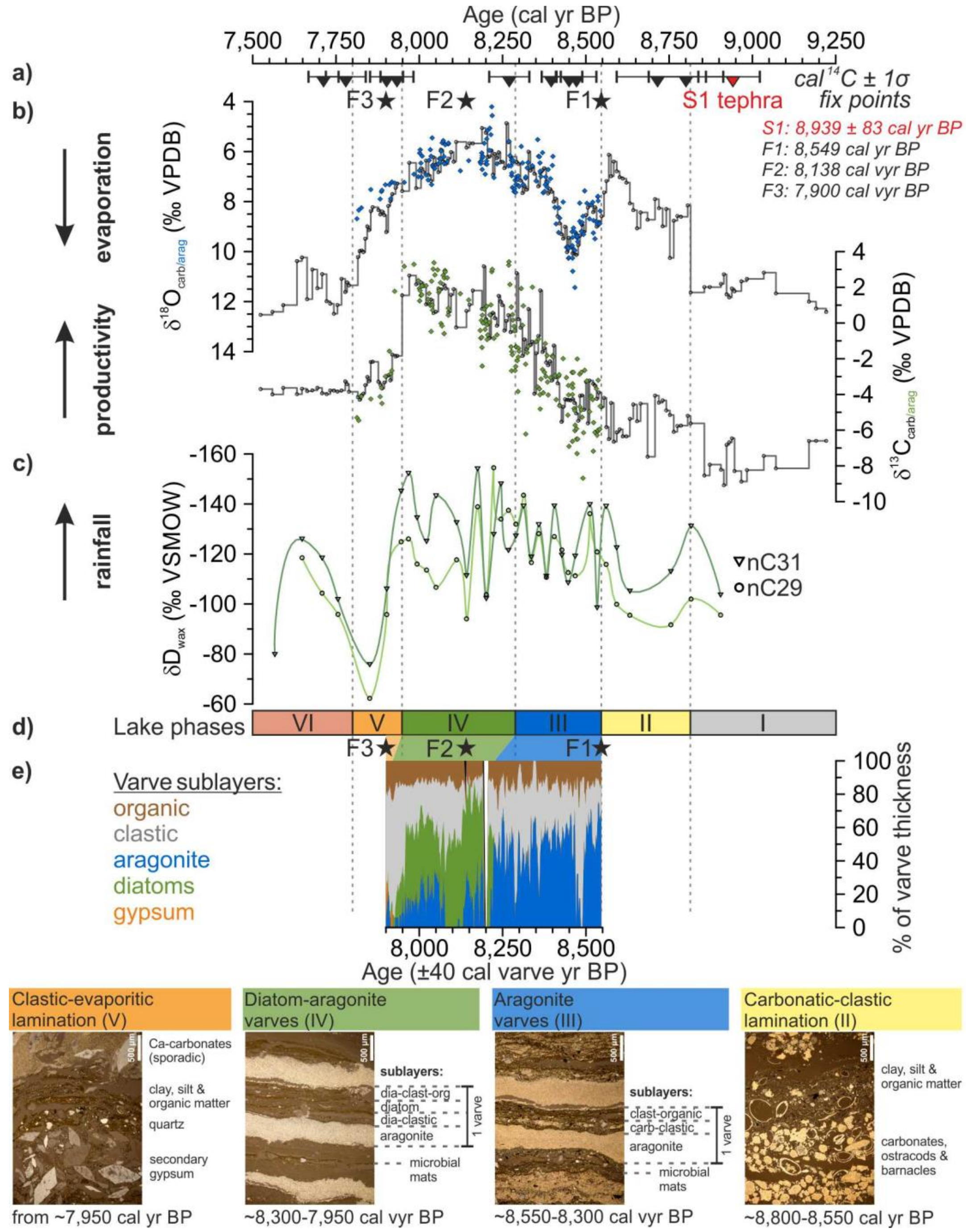

Figure 2: Palaeolake evolution at Tayma between 9,250 and 7,500 cal yr BP. (a) Radiocarbon ages (triangles) and fix points (stars; see Methods); (b) $\delta^{18}O_{carb/arag}$ and $\delta^{13}C_{carb/arag}$ measured on bulk carbonates (solid lines) and on single aragonite layers (blue and green diamonds); (c) δD_{wax} of *n*-alkanes nC_{31} and nC_{29}; (d) Tayma lake phases I–VI; (e) varve sublayers expressed as % of varve thickness for the varve chronology 8,550–7,900 ± 40 cal varve yr BP, and microscope photographs of thin sections highlighting different micro-facies of lake phases II–V.

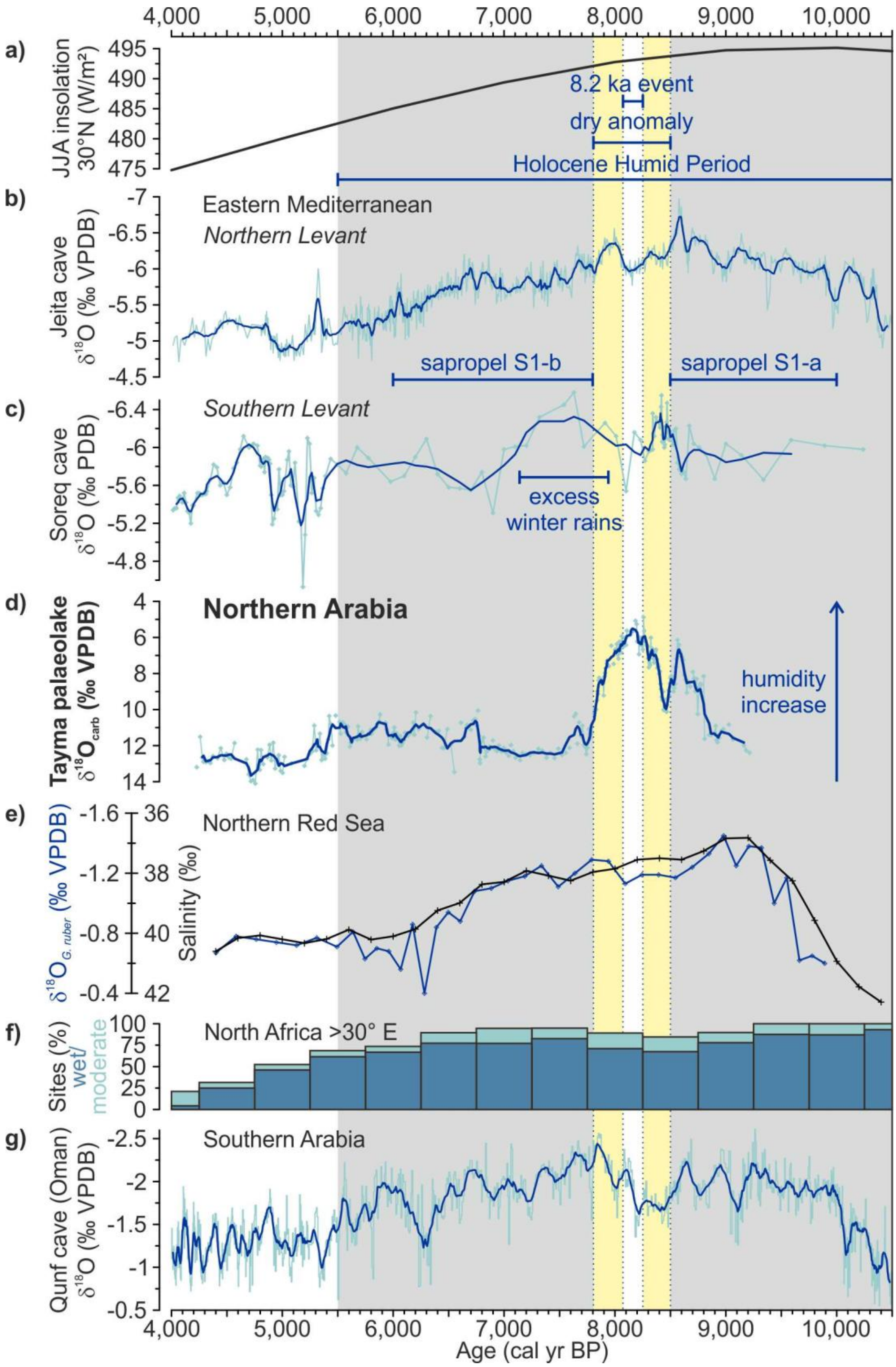

Figure 3: Oxygen isotopes recording humidity changes during the early to middle Holocene Humid Period (HHP) across the E Mediterranean to S Arabia regions. (a) Summer insolation at

30°N[49], duration of the HHP[17] (grey), of the low-latitude dry anomaly[39] (yellow), and of the 8.2 ka cold event in Greenland ice cores[50] (white bar); (b) speleothem $\delta^{18}O$ from Jeita cave (Lebanon)[27], and (c) Soreq cave (Israel)[25,26], with timing of sapropel formation in the E Mediterranean Sea and winter-rain excess in the S Levant[42]; (d) $\delta^{18}O_{carb}$ from Tayma palaeolake (this study); (e) $\delta^{18}O_{\textit{G. ruber}}$ reflecting temperature, and calculated salinity changes from the N Red Sea[13]; (f) frequency histograms of lake records reflecting wet or moderately wet conditions in the E African monsoon domain >30°E[17]; (g) speleothem $\delta^{18}O$ from Qunf cave (Oman)[28]. All $\delta^{18}O$ scales are reversed to reflect higher humidity upwards.

Methods

Tayma sediment cores. Drilling on today's sabkha of the Tayma palaeolake basin was performed in 2011 and 2013 using an Atlas Copco vibracoring device (Cobra mk1) fitted with closed steel auger heads and PVC liners with a diameter of 5 cm. Two series of ca. 6 m long sediment cores (Tay 220/221 and Tay 253/254/255/256) capturing the entire Holocene sequence and reaching down to Ordovician sandstone (Qasim Formation) were obtained in close vicinity ('mastercores' in Supplementary Fig. 1a). They each consist of two parallel, overlapping core sequences A and B with 1 m-long core sections. The cores were opened and photographically documented at the University of Cologne (Laboratory for Physical Geography) and GFZ Potsdam, Germany. The construction of composite profiles and correlation of the sediment cores is based on 24 macroscopic lithological marker layers (fixed marker horizons, FMH).

Tayma sediment cores were analysed for their sedimentology (XRF [X-ray fluorescence] core scanning, quantitative XRF on discrete samples, semi-quantitative XRD [X-ray diffraction], micro-facies analyses on thin sections), geochemistry (elemental analyses, stable isotopes, lipid biomarkers), palynology (vegetation reconstruction through pollen analysis) and micropalaeontology (assemblages of foraminifera, ostracods and diatoms). Here we used stable isotopes of oxygen and carbon ($\delta^{18}O$ and $\delta^{13}C$) measured on primary carbonates in combination with micro-facies analyses of annually laminated (varved) sediments to trace the evolution of the early to mid-Holocene palaeolake at Tayma. Further proxy data have partially been published[4,35,51], or will be presented in forthcoming publications.

In Supplementary Fig. 6, the lithological profile of the ca. 6.5 m-long composite core, TOC (total organic carbon) content[51], $\delta^{18}O_{carb}$ and $\delta^{13}C_{carb}$ (see methodological details further down), and statistical clustering results of the XRF core-scanning record are shown. The elemental composition of the sediment core was determined by non-destructive XRF core scanning on the split-core sediment surface using an ITRAX elemental scanner at GFZ Potsdam. Measurements were obtained every 0.2 mm using a Cr X-ray source, operated at 30 kV, 30 mA and 10 s, to capture intensities of the elements Si, S, Cl, K, Ca, Ti, Fe, Sr and Zr. A centred log-ratio (clr = ln [element intensity/geometric mean of all nine elements]) transform was performed for all elements of each measurement to eliminate the influences of physical properties, sample geometry and matrix effects[52,53] and to enable robust statistical analyses[54].

The sediments deposited in the Tayma basin are mainly composed of clay, silt and sand, evaporites (sulphates), authigenic carbonates and in parts high amounts of diatoms, ostracods and foraminifera (Supplementary Fig. 6). Clay- and silt-sized detritus is dominant in the core and was deposited as dark grey, mm- to cm-thick, occasionally graded layers. Coarser silt- to sand-sized minerals (mainly quartz) are scattered in the sediments or are concentrated in the uppermost part of the Tayma profile. Evaporites were mainly identified in the form of whitish-beige, finer-grained laminae or post-depositionally grown, large crystals of gypsum and other sulphates. Carbonates are present in the form of white, sub-mm thick primary aragonite laminae, biogenic calcite (ostracods, foraminifera, and barnacle and gastropod shell fragments) and primary magnesium-calcite layers.

Statistical clustering (Ward's method) of XRF core-scanning results indicates four main sediment groups (Supplementary Fig. 6): Cluster 1 (light grey) is dominated by Si, Ti and Fe and describes the siliciclastic sediments and occurs predominantly in the upper part of the Tayma profile (VII – sabkha phase). Cluster 2 (green) does not show a clear preference, but is rather a mixture of all considered elements, describing clastic, carbonate and evaporitic 'background' sediments. Cluster 3 (blue) is dominated by Sr and Ca and describes aragonite, which occurs exclusively in the varved sediments of the Tayma core representing the deep-lake phases III and IV (Fig. 2e). Cluster 4 (orange) is dominated by the elements S and Ca and mainly describes gypsum that was deposited during the terminal lake phase (V) and thereafter, when wetlands occupied the Tayma basin (phase VI).

Varve micro-facies analysis. We used changes in varve micro-facies, *i.e.* the composition of seasonal sublayers of the annual laminations, to infer changing seasonality and the interannual variability of lake-internal evaporation and productivity. The thickness and composition of varve sublayers were analysed under the microscope along with varve counting on petrographic thin sections. A total of eleven different sublayer types were grouped into five main sediment components (carbonate, organic, clastic, diatoms and gypsum). Data are given as relative contribution (in %) to the varve thickness (Fig. 2e). Raw data of micro-facies sub-layer thicknesses are presented in Supplementary Fig. 9.

Age model construction. Due to the absence of datable terrestrial macroscopic plant remains in Tayma cores and reported hard-water effects altering radiocarbon ages from gastropods, ostracods and *Ruppia* seeds for up to 1,500 years[4,15], preliminary age models[4,51] were based on AMS radiocarbon dating of pollen grains, as these are unsusceptible for incorporating old carbon[55,56]. Pollen extraction from a total of 33 samples of 1–13 cm long sediment sections followed a combination of physical and chemical separation protocols[55–58]. Sample preparation included sieving (at 6, 20, 40 and 70 µm), treatment with heated HCl, KOH and H_2SO_4, and heavy-liquid density separation using CsCl and sodium polytungstate.

Varve counting was performed on 14 large-scale (10 cm x 1.5 cm) petrographic thin sections using a Leica DMLP petrographic microscope under semi-/fully polarised light and with 50x magnification. Thin sections were prepared following standard procedures for soft sediments[59] including freeze-drying and impregnation with epoxy resin (Araldite 2020). Sawing and polishing were performed manually under dry conditions to avoid salt crystallisation. Multiple counting and the definition of correlation marker layers ensured a negligible subjective counting error. Counting uncertainty due to poor sublayer quality is ± 40 varves (6.2%).

The age-depth model was constructed with Bacon v2.2 using flexible Bayesian modelling[60] including implemented outlier analysis and the IntCal13 atmospheric calibration curve[61]. All 38 radiocarbon ages of pollen concentrates, other plant remains (*Ruppia* seeds, non-pollen palynomorphs, charred plant particles), two mollusc samples, as well as a tephrochronological anchor identified close to the base of the Tayma sediment record (the central Anatolian 'S1'-tephra dated at 8,983 ± 83 cal yr BP in the Dead Sea)[34], were considered for age modelling. The floating varve chronology of 650 ± 40 varve years served to refine the Bayesian model within the varved section. The start of varve formation is defined by ^{14}C dating to 8,549 cal yr BP (8,470–8,605 cal yr BP for the 95.4% probability range). Based on this fix point (F1), the varve age of a turbidite layer at 8,138 ± 40 varve years BP and the end of varve formation at 7,900 ± 40 varve years BP were used as further fix points (F2 and F3) in the adjusted Bayesian model (Supplementary Fig. 7).

Outlier analysis reliably discarded samples (n = 6) containing ≤50% pollen or hard-water-affected material (gastropod shells, *Ruppia* seeds), and 13 samples with ≥50% pollen unsuitable for the Bayesian age-depth model. All remaining 18 ^{14}C ages of pollen concentrates included in the final model contained high pollen concentrations of at least 50% (Supplementary Table 1, Supplementary Fig. 7).

Reconstruction of hydroclimatic conditions. The stable isotope composition of $\delta^{18}O$ and δD of lake water in closed lakes is mainly controlled by precipitation and evaporation and reflects hydrological changes and moisture sources[62]. The $\delta^{18}O_{carb/arag}$ ($\delta^{13}C$) values of lake carbonates and δD_{wax} from fossil leaf waxes in lake sediments are proxies for hydroclimatic conditions and were used to reconstruct the precipitation, lake-water evaporation and temperature during the early to mid-Holocene. To assess the hydrological balance of the Tayma palaeolake (8,800–7,950 cal yr BP), the wetland (7,800-6,800 cal yr BP), and the potential moisture sources during the HHP, we compared calculated δD_p (precipitation) and $\delta^{18}O_{water}$ (lake water) values with the isotopic characterization of the main regional atmospheric systems, recent precipitation, as well as surface and groundwater isotope compositions (Supplementary Fig. 8).

Stable oxygen and carbon isotope measurements ($\delta^{13}C_{carb}$ and $\delta^{18}O_{carb}$) were performed on the carbonate fraction of a total of 262 freeze-dried and ground samples taken in cm slices from core Tay 220. Bulk samples of ~0.4 mg were loaded into 10 ml Labco Exetainer vials, automatically flushed with He and reacted in phosphoric acid (100%) at 75 °C for 60 min[63]. The stable isotope compositions were determined at GFZ Potsdam using a Finnigan GasBenchII with carbonate option coupled to a DELTAplusXL IRMS (isotope ratio mass spectrometer) (ThermoFisher Scientific). For $\delta^{18}O_{arag}$ and $\delta^{13}C_{arag}$ determination on 165 single aragonite laminae, about 0.06 mg per lamina was taken from dried and impregnated sediment blocks by drilling. For the isotope measurements of ostracods ($\delta^{18}O_{ostr}$ and $\delta^{13}C_{ostr}$), intact valves of adult specimens of *Cyprideis torosa* (Jones, 1850) were hand-picked from the wet-sieved and dried sediment fraction >125 µm. Aragonite and ostracod samples were measured at GFZ Potsdam with an automated carbonate device (KIEL IV) coupled to a Finnigan MAT253 IRMS (ThermoFisher Scientific) on cryogenically purified CO_2 released by dissolution with 103% H_3PO_4 at 72 °C. Oxygen and carbon isotope compositions are given relative to the VPDB (Vienna Peedee Belemnite) standard in conventional delta notation δ (‰). Calibration was performed using international reference standards (NBS18 and NBS19). For both methods, standard deviations (1σ) for reference and replicate analyses are better than 0.08‰ for $\delta^{18}O$ and $\delta^{13}C$.

In closed lakes, $\delta^{18}O_{carb}$ values mainly reflect hydrological changes and are used as a proxy for precipitation, groundwater influx and lake evaporation because: (i) seasonality and temperature have little effect on oxygen isotope fractionation of precipitation in low-latitude regions[62,64]; (ii) the lake water oxygen isotopic composition in an endorheic basin is governed by evaporation under arid climate conditions resulting in increased $\delta^{18}O_{water}$; (iii) equilibrium oxygen isotope fractionation is assumed for inorganic carbonates; and (iv) primary inorganic carbonates precipitate during the spring-summer season induced by evaporation and/or phytoplankton bloom in the epilimnion. The latter is consistent with increasing $\delta^{13}C_{carb}$ values, indicating ^{12}C depletion of the total dissolved inorganic carbon (TDIC) due to atmospheric release and/or preferential use of aquatic plants.

The calculation of $\delta^{18}O_{VSMOW}$ palaeolake water from the carbonate $\delta^{18}O_{VPDB}$ values using the re-expressed relationship of ref[65] in the simplified eq. (1) according to ref[62]:

$$(1)\ T°C=13.8–4.58(\delta c–\delta w)$$

under equilibrium water-calcite precipitation at 21 °C (as average temperature in spring) and an offset of +0.6‰ for aragonite and magnesium bearing calcite reveals comparable $\delta^{18}O$ values between precipitated carbonates and host water. The modelled mean $\delta^{18}O_{water}$ for the palaeolake water is high with +8.4‰ and, thus, significantly lighter due to freshwater inflow of surface and groundwater than for the wetland with a calculated mean $\delta^{18}O_{water}$ of +13.1‰ due to lower precipitation and high evaporation.

Stable hydrogen isotopes of leaf-wax *n*-alkanes (δD_{wax}) were measured on 64 samples from core Tay 255. Samples were taken in 1 cm-slices, freeze-dried and grounded for lipid biomarkers extraction at the Max Planck Institute (MPI) for Biogeochemistry in Jena. 5–15 g of the sample was extracted using a 40 ml dichloromethane:methanol (9:1) mixture at 100 °C and 120 bar for 15 min in two consecutive cycles using a BÜCHI SpeedExtractor. The total lipid extract was separated into aliphatic, aromatic and alcohol/fatty acid fractions using solid-phase extraction on silica gel according to the method presented in ref[66]. The aliphatic hydrocarbon fraction was desulfurized using HCl-activated copper (15% HCl). Identification and quantification of *n*-alkanes were accomplished using a GC-MS (Agilent Technologies, 7890A GC-System; 220 Ion trap MS) by comparing peak areas and retention times with an external *n*-alkane standard mixture (*n*C16 to *n*C36). Compound-specific hydrogen isotope ratios (expressed as δD) of the *n*-alkanes were measured on a DELTA V^{plus} Isotope Ratio Mass Spectrometer (IRMS; Thermo Scientific) coupled to an Agilent 7890 GC (Agilent Technologies) at GFZ Potsdam. Every sample was measured in triplicates. The mean standard deviation of all measured samples was 3‰. The δD values were normalized to the Vienna Standard Mean Ocean Water (VSMOW).

The changes in δD_{wax} of the lake records are interpreted as indicator for the variability in precipitation, humidity and vegetation type[64,66]. Hydrogen isotopes δD_{wax} of leaf wax nC_{29} and nC_{31} *n*-alkanes were used to calculate δD_p between precipitation (p) according to refs[36,37]. The negative isotopic fractionation from δD_p to δD_{wax} due to the incorporation of hydrogen in leaf waxes has been calculated using eq. (2):

(2) $$\delta D_p = [(\delta D_{wax}+1000)/((\varepsilon/1000)+1)]-1000$$

with ε = -130 for nC_{29} and nC_{31} *n*-alkanes representing the mixture of C3/C4 plant waxes of grasses, shrubs and trees[4] (Supplementary Fig. 8). Following ref[5], we inferred the precipitation rate from δD_p values. The relationship of precipitation and rainfall amount for the Sahara region described a non-linear dependence with a steep slope in δD_p values below 100 mm/a and a strong influence of the amount effect.

δ^{18}O and δD isotopes of water samples. Filtered water samples of groundwater from the historical Bir Haddaj well of the Tayma oasis, from the Tay 255 borehole in the palaeolake, and evaporated rainwaters from small water pools south of the palaeolake taken shortly after a rain event in December 2015, were triple-measured for $\delta^{18}O_{water}$ and δD_{water} relative to VSMOW using Cavity Ring-Down spectrometers (PICARRO L2120-i and L2130-I). Analytical precision of VSMOW and SLAP calibrated analyses was <1‰ for both, $\delta^{18}O_{water}$ and δD_{water}.

The isotopic fractionation of lake-water evaporation was calculated for the remaining lake water ($\delta^{18}O_{rw}$) using initial groundwater-supported lake water with $\delta^{18}O_{iw}$ of -3‰ with simple Rayleigh distillation after eq. (3):

(3) $\delta^{18}O_{rw}=\delta^{18}O_{iw}-1000(f^{(\alpha-1)}-1)$

where α = fractionation factor between water and vapor at 21 °C[67] and f = fraction of remaining lake water.

Reconstruction of palaeo-moisture source and lake-water evaporation. The few meteoric water samples from Tabuk (IAEA) plot with $\delta^{18}O$ ~-1‰ closely to the global meteoric water line (GMWL), except for one lighter sample tending more to the Eastern Mediterranean meteoric water line (EMMWL). Recent (12/2015) evaporated rainwater samples collected in water pools in a wadi SW of the Tayma palaeolake show $\delta^{18}O$ values of around -0.5‰ and slightly enriched δD values. Using δD_{wax} to estimate past precipitation rates reveals the lowest values of about -2‰ δD_{water} for the wetland phase and values as low as -28‰ for the palaeolake (Supplementary Fig. 8), indicating higher rainfall amounts between 8,800 and 7,950 cal yr BP due to increasing precipitation and a probable amount effect.

The stable isotopes of the Bir Haddaj well in Tayma reflect subsurface groundwater with -3.5‰ $\delta^{18}O$ and -24.6‰ δD, similar to the middle of the Saq aquifer[68,69]. The water from the palaeolake sampled in 1.5 m depth of the well Tay 255 in 2015 with +7.4‰ $\delta^{18}O$ and +16.2‰ δD probably reflects pore-water isotope composition. The portion of surface-water evaporation along the slope between -3‰ $\delta^{18}O_{iw}$ and the Tay 255 well reaches about 70% for the deep lake phase and

>80% for the wetland phase. The isotopic difference between the deep palaeolake and the wetland water is mainly influenced by decreases in precipitation and increasing evaporation. Although the three atmospheric systems affecting the NW Arabian Peninsula (Indian Monsoon, Mediterranean Westerlies and African Monsoon) show isotopic fingerprints with more or less variation and deuterium excess, it is unreasonable to decipher the moisture sources during the time of palaeolake formation due to the determination of precipitation using δD_{wax} and $\delta^{18}O_{carb}$ being indirect, as well as associated fractionation effects. In general, the moisture source-related isotope fingerprints over the Arabian Peninsula are masked by strong evaporation, continental and altitude effects, sub-cloud evaporation, moisture recycling and the amount effect[70].

References

1. Jennings, R. P. et al. The greening of Arabia: Multiple opportunities for human occupation of the Arabian Peninsula during the Late Pleistocene inferred from an ensemble of climate model simulations. *Quat. Int.* **382**, 181-199 (2015).

2. Parton, A. et al. Alluvial fan records from southeast Arabia reveal multiple windows for human dispersal. *Geology* **43**, 295-298 (2015).

3. Breeze, P. S. et al. Palaeohydrological corridors for hominin dispersals in the Middle East ~250–70,000 years ago. *Quat. Sci. Rev.* **144**, 155-185 (2016).

4. Dinies, M., Plessen, B., Neef, R. & Kürschner, H. When the desert was green: Grassland expansion during the early Holocene in northwestern Arabia. *Quat. Int.* **382**, 293-302 (2015).

5. Tierney, J. E., Pausata, F. S. R. & deMenocal, P. B. Rainfall regimes of the Green Sahara. *Sci. Adv.* **3**, e1601503 (2017).

6. Nicholson, S. L., Hosfield, R., Groucutt, H. S., Pike, A. W. & Fleitmann, D. Beyond arrows on a map: The dynamics of *Homo sapiens* dispersal and occupation of Arabia during Marine Isotope Stage 5. *J. Anthropol. Archaeol.* **62**, 101269 (2021).

7. Armitage, S. J. et al. The southern route "Out of Africa": Evidence for an early expansion of modern humans into Arabia. *Science* **331**, 453-456 (2011).

8. Gourcutt H. S. et al. *Homo sapiens* in Arabia by 85,000 years ago. *Nature Ecol. Evol.* **2**, 800-809 (2018).

9. Crassard, R. et al. Beyond the Levant: First evidence of a Pre-Pottery Neolithic incursion into the Nefud Desert, Saudi Arabia. *PLOS ONE* **8**, e68061 (2013).

10. Petraglia, M. D., Groucutt, H. S., Guagnin, M., Breeze, P. S. & Boivin, N. Human responses to climate and ecosystem change in ancient Arabia. *P. Natl. Acad. Sci. USA* **117**, 8263-8270 (2020).

11. Crassard, R., Hilbert, Y. H., Preusser, F., Wulf, G. & Schiettecatte, J. Middle Palaeolithic occupations in central Saudi Arabia during MIS 5 and MIS 7: new insights on the origins of the peopling of Arabia. *Archaeol. Anthropol. Sci.* **11**, 3101-3120 (2019).

12. Guagnin, M. et al. Rock art imagery as a proxy for Holocene environmental change: A view from Shuwaymis, NW Saudi Arabia. *Holocene* **26**, 1822-1834 (2016).

13. Arz, H. W., Lamy, F., Pätzold, J., Müller, P. J. & Prins, M. Mediterranean moisture source for an Early-Holocene Humid Period in the northern Red Sea. *Science* **300**, 118-121 (2013).

14. Enzel, Y., Kushnir, Y. & Quade, J. The middle Holocene climatic records from Arabia: Reassessing lacustrine environments, shift of ITCZ in Arabian Sea, and impacts of the southwest Indian and African monsoons. *Global Planet. Change* **129**, 69-91 (2015).

15. Engel, M. et al. Lakes or wetlands? A comment on 'The middle Holocene climatic records from Arabia: Reassessing lacustrine environments, shift of ITCZ in Arabian Sea, and impacts of the southwest Indian and African monsoons' by Enzel et al. *Global Planet. Change* **148**, 258-267 (2017).

16. Kutzbach, J. E. & Liu, Z. Response of the African Monsoon to orbital forcing and ocean feedbacks in the middle Holocene. *Science* **278**, 440-443 (1997).

17. Shanahan, T. M. et al. The time-transgressive termination of the African Humid Period. *Nat. Geosci.* **8**, 140-144 (2015).

18. Kutzbach, J. E., Chen, G., Cheng, H., Edwards, R. L. & Liu, Z. Potential role of winter rainfall in explaining increased moisture in the Mediterranean and Middle East during periods of maximum orbitally-forced insolation seasonality. *Clim. Dyn.* **42**, 1079-1095 (2014).

19. Rubin, S., Ziv, B. & Paldor, N. Tropical plumes over eastern North Africa as a source of rain in the Middle East. *Mon. Weather Rev.* **135**, 4135-4148 (2007).

20. Tubi, A., Dayan, U. & Lensky, I. M. Moisture transport by tropical plumes over the Middle East: a 30-year climatology. *Q. J. Roy. Meteorol. Soc.* **143**, 3165-3176 (2017).

21. Waldmann, N., Torfstein, A. & Stein, M. Northward intrusions of low- and mid-latitude storms across the Saharo-Arabian belt during past interglacials. *Geology* **38**, 567-570 (2010).

22. Skinner, C. B. & Poulsen, C. J. The role of fall season tropical plumes in enhancing Saharan rainfall during the African Humid Period. *Geophys. Res. Lett.* **43**, 349-358 (2016).

23. Hausleiter, A., Eichmann, R. & Al-Najem, M. (eds.). *Taymā' I* (Archaeopress, Oxford, 2018).

24. Breeze, P. S. et al. Remote sensing and GIS techniques for reconstructing Arabian palaeohydrology and identifying archaeological sites. *Quat. Int.* **382**, 98-119 (2015).

25. Bar-Matthews, M., Ayalon, A., Gilmour, M., Matthews, A. & Hawkesworth, C. J. Sea–land oxygen isotopic relationships from planktonic foraminifera and speleothems in the Eastern Mediterranean region and their implication for paleorainfall during interglacial intervals. *Geochim. Cosmochim. Acta* **67**, 3181-3199 (2003).

26. Grant, K. M. et al. Rapid coupling between ice volume and polar temperature over the past 150,000 years. *Nature* **491**, 744-747 (2012).

27. Cheng, H. et al. The climate variability in northern Levant over the past 20,000 years. *Geophys. Res. Lett.* **42**, 8641-8650 (2015).

28. Fleitmann, D. et al. Holocene ITCZ and Indian monsoon dynamics recorded in stalagmites from Oman and Yemen (Socotra). *Quat. Sci. Rev.* **26**, 170-188 (2007).

29. Cheng, H. et al. Timing and structure of the 8.2 kyr B.P. event inferred from $\delta^{18}O$ records of stalagmites from China, Oman, and Brazil. *Geology* **37**, 1007-1010 (2009).

30. Schulz, E. & Whitney, J. W. Upper Pleistocene and Holocene lakes in the An Nafud, Saudi Arabia. *Hydrobiologia* **143**, 175-190 (1986).

31. Rosenberg, T. M. et al. Middle and Late Pleistocene humid periods recorded in palaeolake deposits of the Nafud desert, Saudi Arabia. *Quat. Sci. Rev.* **70**, 109-123 (2013).

32. Zielhofer, C. et al. Climate forcing and shifts in water management on the Northwest Arabian Peninsula (mid-Holocene Rasif wetlands, Saudi Arabia). *Quat. Int.* **473**, 120-140 (2018).

33. Engel, M. et al. The early Holocene humid period in NW Saudi Arabia – sediments, microfossils and palaeo-hydrological modelling. *Quat. Int.* **266**, 131–141 (2012).

34. Neugebauer, I. et al. Implications of S1 tephra findings in Dead Sea and Tayma palaeolake sediments for marine reservoir age estimation and palaeoclimate synchronisation. *Quat. Sci. Rev.* **170**, 269-275 (2017).

35. Pint, A. et al. How to discriminate athalassic and marginal marine microfaunas: Foraminifera and other fossils from an early Holocene continental lake in northern Saudi Arabia. *J. Foram. Res.* **47**, 175-187 (2017).

36. Sachse, D. et al. Molecular paleohydrology: interpreting the hydrogen-isotopic composition of lipid biomarkers from photosynthesizing organisms. *Annu. Rev. Earth Pl. Sc.* **40**, 221-249 (2012).

37. Collins, J. A. et al. Estimating the hydrogen isotopic composition of past precipitation using leaf-waxes from western Africa. *Quat. Sci. Rev.* **65**, 88-101 (2013).

38. Arz, H. W., Lamy, F., Pätzold, J. A pronounced dry event recorded around 4.2 ka in brine sediments from the northern Red Sea. *Quat. Res.* **66**, 432-441 (2006).

39. Rohling, E. J. & Palike, H. Centennial-scale climate cooling with a sudden cold event around 8,200 years ago. *Nature* **434**, 975-979 (2005).

40. Gasse, F. Hydrological changes in the African tropics since the Last Glacial Maximum. *Quat. Sci. Rev.* **19**, 189-211 (2000).

41. Blanchet, C. L. et al. High- and low-latitude forcing of the Nile River regime during the Holocene inferred from laminated sediments of the Nile deep-sea fan. *Earth Planet. Sci. Lett.* **364**, 98-110 (2013).

42. Rohling, E. J., Marino, G. & Grant, K. M. Mediterranean climate and oceanography, and the periodic development of anoxic events (sapropels). *Earth Sci. Rev.* **143**, 62-97 (2015).

43. Tesi, T. et al. Large-scale response of the Eastern Mediterranean thermohaline circulation to African monsoon intensification during sapropel S1 formation. *Quat. Sci. Rev.* **159**, 139-154 (2017).

44. Pross, J. et al. Massive perturbation in terrestrial ecosystems of the Eastern Mediterranean region associated with the 8.2 kyr BP climatic event. *Geology* **37**, 887-890 (2009).

45. Fick, S. E. & Hijmans, R. J. WorldClim 2: new 1-km spatial resolution climate surfaces for global land areas. *Int. J. Climatol.* **37**, 4302-4315 (2017).

46. Akçar, N. & Schlüchter, C. Paleoglaciations in Anatolia: A schematic review and first results. *E&G Quat. Sci. J.* **55**, 102-121 (2005).

47. Wellbrock, K., Strauss, M., Külls, C. & Grottker, M. in *Des refuges aux oasis: Vivre en milieu aride de la Préhistoire à aujourd'hui. XXXVIIIe rencontres internationales d'archéologie et d'histoire d'Antibes* (eds. Purdue, L., Charbonnier, J. & Khalidi, L.) 231-249 (Éditions APDCA, 2018).

48. Danielson, J. J. & Gesch, D. B. Global multi-resolution terrain elevation data 2010 (GMTED2010). *USGS Open-File Rep.* **2011–1073** (2011).

49. Laskar, J. et al. A long-term numerical solution for the insolation quantities of the Earth. *Astron. Astrophys.* **428**, 261-285 (2004).

50. Thomas, E. R. et al. The 8.2 ka event from Greenland ice cores. *Quat. Sci. Rev.* **26**, 70-81 (2007).

51. Dinies, M., Neef, R., Plessen, B. & Kürschner, H. in *The Archaeology of North Arabia: Oases and Landscapes* (ed. Luciani, M.) 57-78 (Austrian Academy of Sciences Press, 2016).

52. Weltje, G. J. & Tjallingii, R. Calibration of XRF core scanners for quantitative geochemical logging of sediment cores: Theory and application. *Earth Planet. Sci. Lett.* **274**, 423-438 (2008).

53. Weltje, G. J. et al. in *Micro-XRF Studies of Sediment Cores* (eds. Croudace, I. W. & Rothwell R. G.) 507-534 (Springer, Dordrecht, 2015).

54. Aitchison, J. The statistical analysis of compositional data. *J. R. Stat. Soc. Ser. B* **44**, 139-160 (1982).

55. Brown, T. A., Nelson, D. E., Mathewes, R. W., Vogel, J. S. & Southon, J. R. Radiocarbon dating of pollen by accelerator mass spectrometry. *Quat. Res.* **32**, 205-212 (1989).

56. Vandergoes, M. J. & Prior, C. A. AMS Dating of pollen concentrates – a methodological study of late Quaternary sediments from South Westland, New Zealand. *Radiocarbon* **45**, 479-491 (2003).

57. Regnéll, J. & Everitt, E. Preparative centrifugation – a new method for preparing pollen concentrates suitable for radiocarbon dating by AMS. *Veg. Hist. Archaeobot.* **5**, 201-205 (1996).

58. Nakagawa T. et al. Dense-media separation as a more efficient pollen extraction method for use with organic sediment/deposit samples: comparison with the conventional method. *Boreas* **27**, 15-24 (1998).

59. Brauer, A. & Casanova, J. Chronology and depositional processes of the laminated sediment record from Lac d'Annecy, French Alps. *J. Paleolimnol.* **25**, 163-177 (2001).

60. Blaauw, M. & Christen, J. A. Flexible paleoclimate age-depth models using an autoregressive gamma process. *Bayesian Anal.* **6**, 457-474 (2011).

61. Reimer, P. J. et al. IntCal13 and Marine13 radiocarbon age calibration curves 0–50,000 Years cal BP. *Radiocarbon* **55**, 1869-1887 (2013).

62. Leng, M. J. & Marshall, J. D. Palaeoclimate interpretation of stable isotope data from lake sediment archives. *Quat. Sci. Rev.* **23**, 811-831 (2004).

63. Spötl, C. & Vennemann, T. W. Continuous-flow isotope ratio mass spectrometric analysis of carbonate minerals. *Rapid Comm. Mass Sp.* **17**, 1004-1006 (2003).

64. Bowen, G. J. Isoscapes: spatial pattern in isotopic biogeochemistry. *Annu. Rev. Earth Pl. Sc.* **38**, 161-187 (2010).

65. Kim, S.-T. & O'Neil, J. R. Equilibrium and nonequilibrium oxygen isotope effects in synthetic carbonates. *Geochim. Cosmochim. Acta* **61**, 3461-3475 (1997).

66. Sachse, D., Radke, J. & Gleixner, G. δD values of individual n-alkanes from terrestrial plants along a climatic gradient – implications for the sedimentary biomarker record. *Org. Geochem.* **37**, 469-483 (2006).

67. Horita, J. & Wesolowski, D. J. Liquid-vapor fractionation of oxygen and hydrogen isotopes of water from the freezing to the critical temperature. *Geochim. Cosmochim. Acta* **58**, 3425-3437 (1994).

68. Al-Sagaby, A. & Moallim, A. Isotopes based assessment of groundwater renewal and related anthropogenic effects in water scarce areas: Sand dunes study in Qasim area, Saudi Arabia. *IAEA-TECDOC* **1246**, 221-229 (2001).

69. Alyamani, M. S. Isotopic composition of rainfall and ground-water recharge in the western province of Saudi Arabia. *J. Arid Environ.* **49**, 751-760 (2001).

70. Michelsen, N. et al. Isotopic and chemical composition of precipitation in Riyadh, Saudi Arabia. *Chem. Geol.* **413**, 51-62 (2015).

Supplementary Information for

The unexpectedly short Holocene Humid Period in Northern Arabia

Ina Neugebauer[1,2], Michèle Dinies[3,4], Birgit Plessen[1], Nadine Dräger[1], Achim Brauer[1], Helmut Brückner[5], Peter Frenzel[6], Gerd Gleixner[7], Philipp Hoelzmann[4], Kim Krahn[8], Anna Pint[6], Valérie F. Schwab[7], Anja Schwarz[8], Rik Tjallingii[1] and Max Engel[9,10,*]

1 GFZ German Research Centre for Geosciences, Section Climate Dynamics and Landscape Evolution, Telegrafenberg, 14473 Potsdam, Germany

2 University of Geneva, Department of Earth Sciences, Rue des Maraichers 13, 1205 Genève, Switzerland

3 German Archaeological Institute (DAI), Scientific Department of the Head Office, Im Dol 2-6, 14195 Berlin, Germany

4 Freie Universität Berlin, Institute of Geographical Sciences, Malteser Str. 74-100, 12249 Berlin, Germany

5 University of Cologne, Institute of Geography, Zülpicher Str. 45, 50674 Köln, Germany

6 Friedrich Schiller University Jena, Institute of Earth Sciences, Burgweg 11, 07749 Jena, Germany

7 Max Planck Institute for Biogeochemistry, Research Group Molecular Biogeochemistry, Hans-Knöll-Str. 10, 07745 Jena, Germany

8 Technische Universität Braunschweig, Institute of Geosystems and Bioindication, Langer Kamp 19c, 38106 Braunschweig, Germany

9 Heidelberg University, Institute of Geography, Im Neuenheimer Feld 348, 69120 Heidelberg, Germany

10 Royal Belgian Institute of Natural Sciences, Geological Survey of Belgium, Jennerstraat 13, 1000 Brussels, Belgium

* Corresponding author: Max Engel, max.engel@uni-heidelberg.de

Regional setting of Tayma

The sabkha N of the town of Tayma fills a closed basin overlying Lower Ordovician micaceous siltstones (Qasim Formation), with an extension of approximately 20 km^2 and a hydrological catchment 660 km^2[1,2] (Supplementary Fig. 1). Today, the deepest point of the sabkha is at about 800 m a.s.l. The depression has developed in a NW–SE trending graben structure above the Ordovician Qasim Formation (Supplementary Fig. 1c). The northern rim consists of a staircase of steep, slightly northwards dipping sandstones and micaceous siltstones of this formation with a maximum height at about 860 m a.s.l. (Supplementary Fig. 1a). To the S, the surface gradually rises towards the town situated above the basin at about 830 m a.s.l., from where the underlying Ordovician Saq sandstone continuously rises up to 1000 m a.s.l. These about 600 m-thick medium to coarse-grained sandstones form the main groundwater-bearing layer of the W Peninsula, the Saq aquifer[3] (Supplementary Fig. 1c). The groundwater flow coming from the SE[4] is under artesian pressure due to the graben structure of the Tayma basin. Potential surface waters drain by several small inflows and wadis into the endorheic basin (Supplementary Fig. 1b).

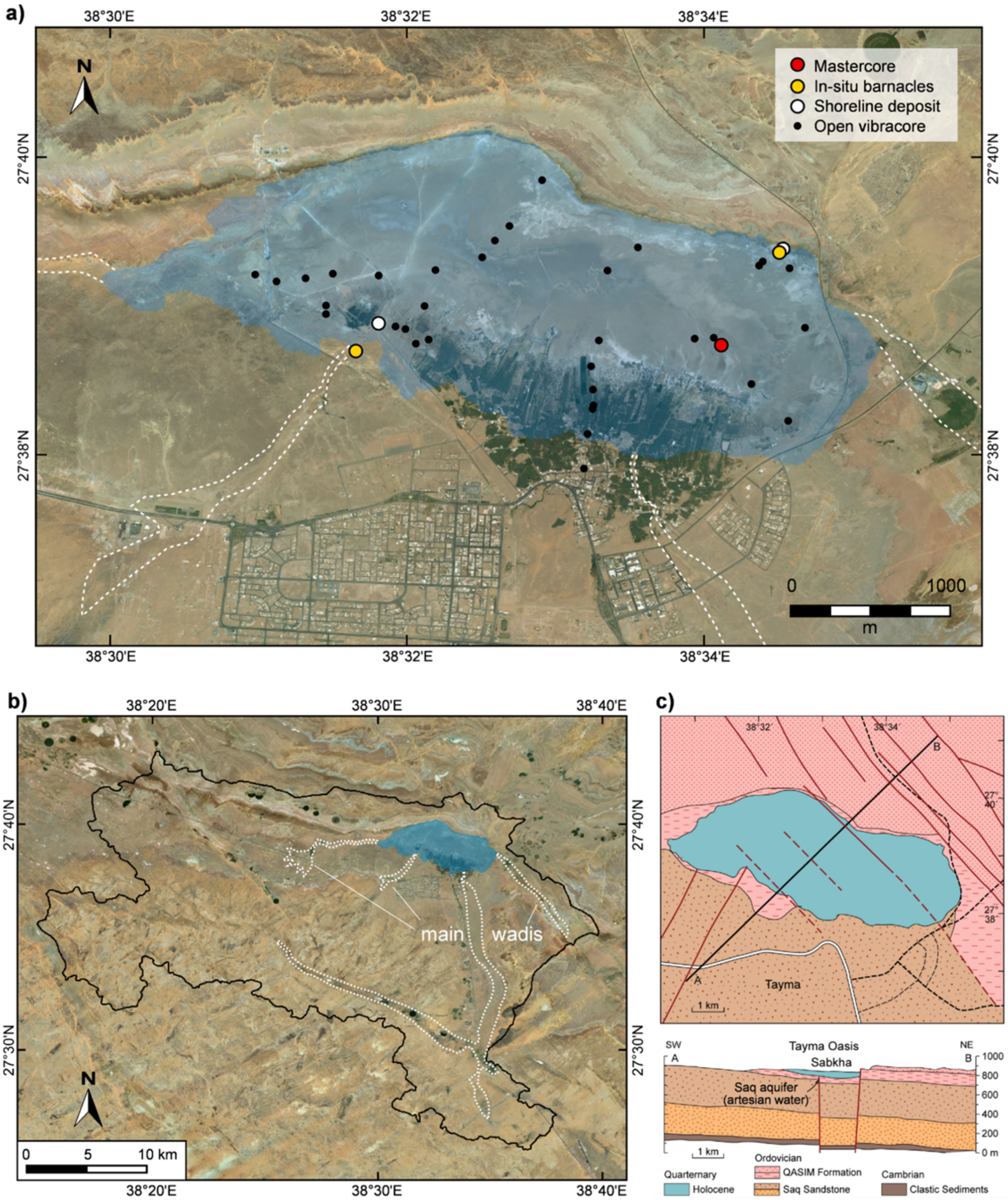

Supplementary Fig. 1: Local setting of the Tayma palaeolake. (a) Tayma palaeolake as reconstructed from highest shoreline deposits[1], a digital elevation model based on local DGNSS and global SRTM data[2] and a large dataset of vibracores (basemap: Landsat/Copernicus, accessed through Google Earth Pro). The main wadis entering the endorheic basin are marked by white dashed lines. (b) Surface catchment of the Tayma palaeolake[5] showing the spatial extent of the main wadis (basemap: Landsat/Copernicus, accessed through Google Earth Pro). (c) Simplified geology and tectonic features of the oasis of Tayma creating the artesian groundwater source, shown as top view and stratigraphic profile based on ref.[6].

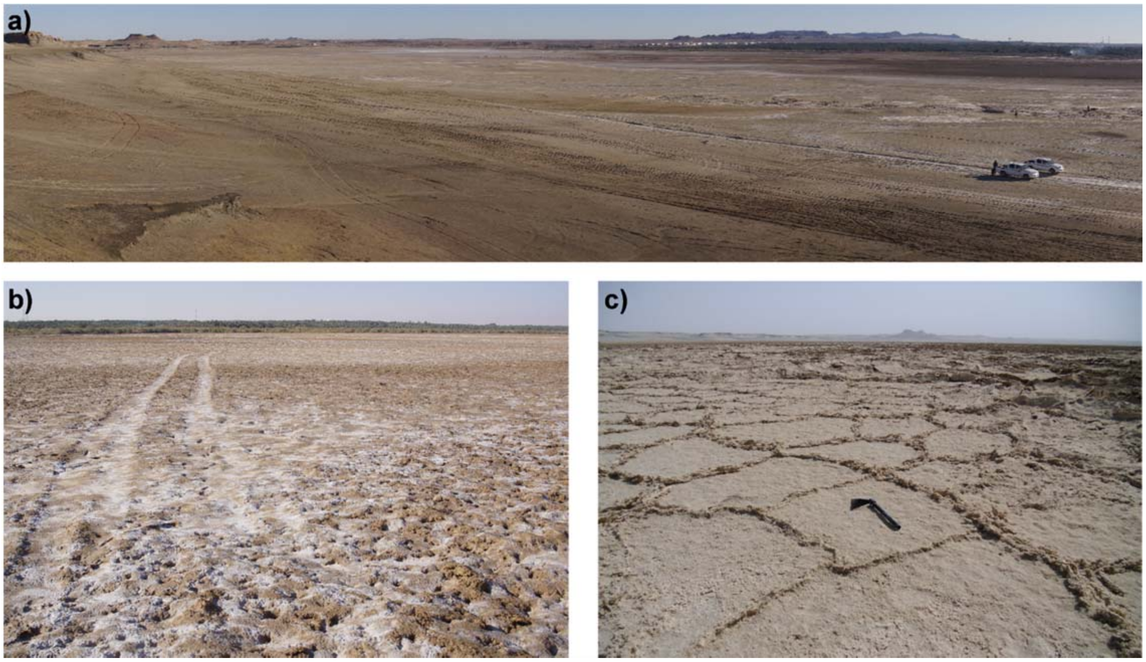

Supplementary Fig. 2: Views of the sabkha of Tayma. (a) Panoramic view from the NW margin on top of the lowermost escarpment towards SE, overlooking the sabkha. Zeugenbergs in the upper left represent remnants of higher escarpment levels. The upper right shows the palm gardens bordering the sabkha in the S as well as some buildings of the easternmost part of the oasis of Tayma. (b) Typical gypsum buckled-crust surface of the central part of the sabkha, thinly covered by Na salts. (c) In some more central parts, the buckled crust gives way to massive salt polygons.

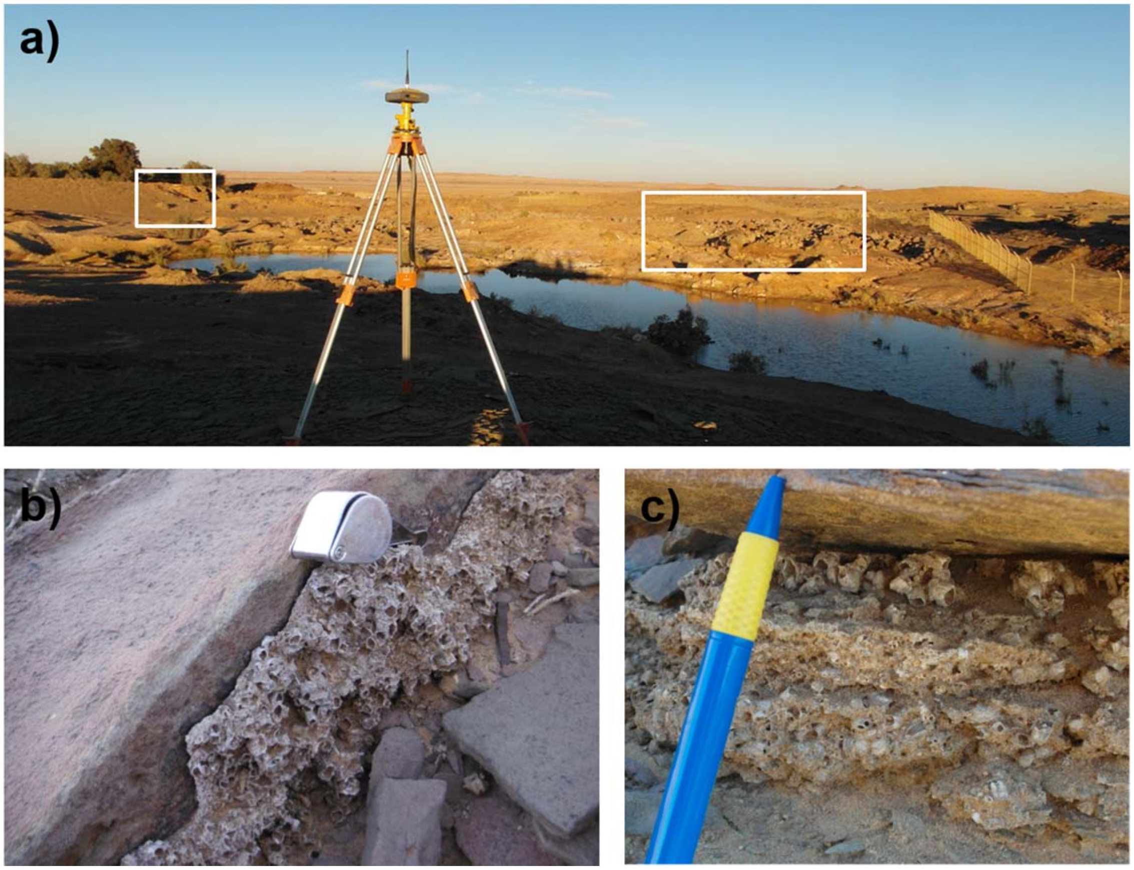

Supplementary Fig. 3: SW barnacle colonies. (a) Overview of the SW major wadi entering the sabkha basin (Supplementary Fig. 1a). (b), (c) Along both wadi margins, *in-situ* Holocene barnacle colonies are preserved at elevations of c. 12 m above the present sabkha floor, representing palaeo-shoreline indicators of the peak phase of the early to mid-Holocene lake (SW yellow dot in Supplementary Fig. 1a).

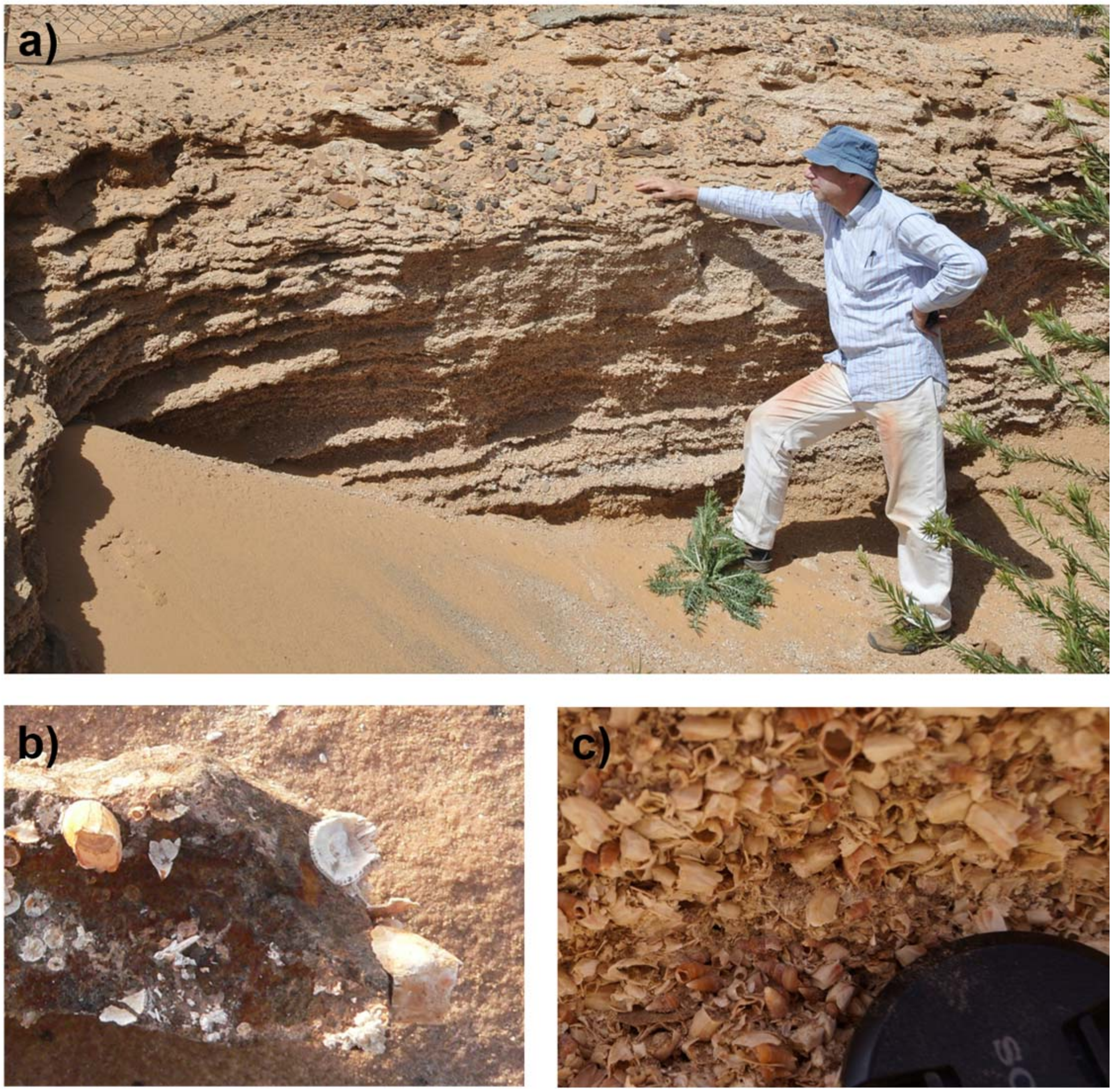

Supplementary Fig. 4: SW bioclastic deposit. (a) Stratified lake-shoreline deposit almost entirely consisting of barnacles, gastropod, ostracod and foraminifer shells and tests, as well as quartz sand (thickness ca. 2.3 m; SW white dot in Supplementary Fig. 1a). Shells were dated to the early Holocene (profile TAY 180 in refs.[1,7]). (b) *In-situ* barnacles attached to local Ordovician siltstone clasts floating in the bioclastic matrix. (c) Close-up of the texture in (a).

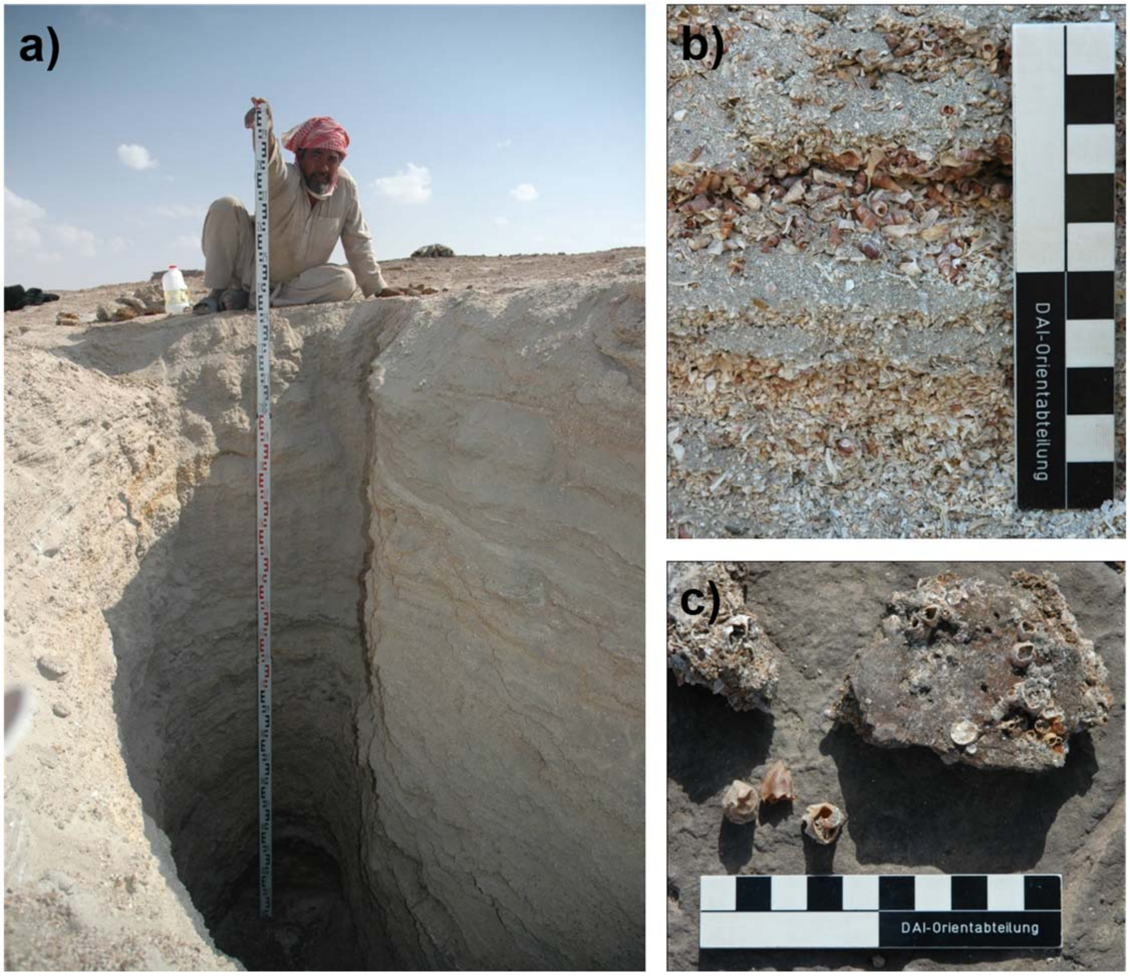

Supplementary Fig. 5: NE bioclastic deposit. (a) Stratified lake-shoreline deposit almost entirely consisting of barnacles, gastropod, ostracod and foraminifer shells and tests, as well as quartz sand (NE yellow and white dots in Supplementary Fig. 1a). Shells were dated to the early Holocene (profile TAY 177 in ref.[1]). (b) Close-up of the texture in (a). (c) *In-situ* Holocene barnacles attached to local Ordovician siltstone at the base of the profile.

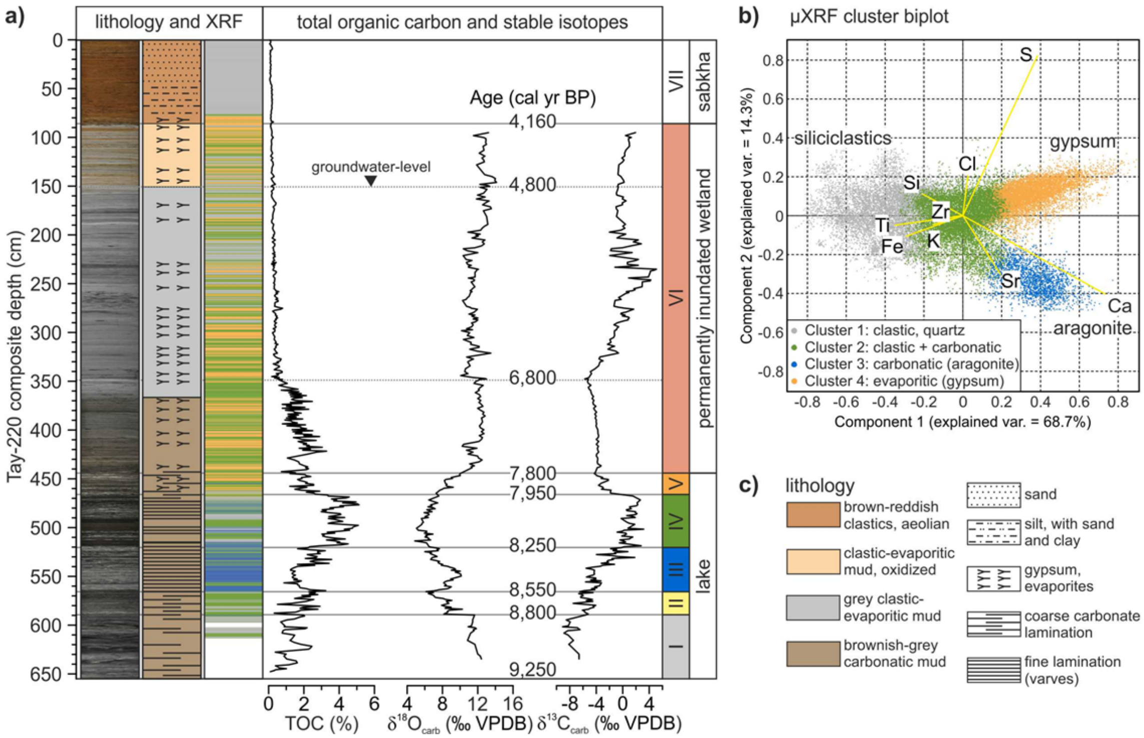

Supplementary Fig. 6: Lithology and sediment geochemistry of the Tayma composite profile. (a) Core scans, lithological description, down-core clustering results from XRF elemental scanning data (see (b) for legend), total organic carbon content (TOC)[8], $\delta^{18}O_{carb}$ and $\delta^{13}C_{carb}$ stable isotopes data, and discrimination of lake phases; the recent (in 2015) groundwater level at 1.5 m depth is marked with black triangles. (b) Principal-component biplot of XRF core-scanning results showing the statistical clusters; principal components 1+2 explain 83% of the variance. (c) Legend for the lithological description.

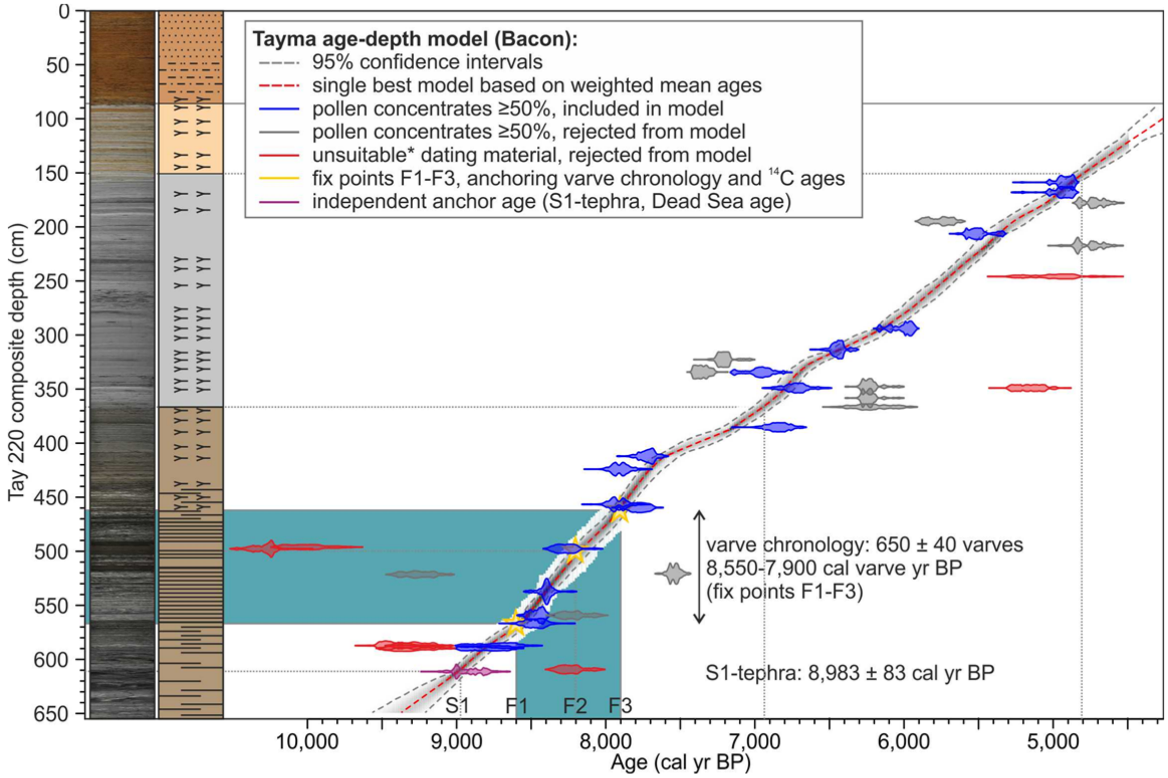

Supplementary Fig. 7: Age-depth model of the Tayma sediment composite profile. The age-depth model was constructed with Bacon v2.2 using flexible Bayesian modelling[9] including implemented outlier analysis and the IntCal13 atmospheric calibration curve[10] (see Methods). The model is based on radiocarbon ages of pollen concentrates, an independent anchor age of the S1-tephra[11] and a varve chronology between 8,550 and 7,900 cal varve yr BP (Tayma deep-lake phases III and IV; marked with a blue rectangle).

Supplementary Table 1: AMS-radiocarbon dating results from Tayma sediment cores. Bold font: sample age included in Bayesian age model (Bacon with implemented outlier analysis); normal font: sample material is suitable (pollen concentration ≥50%), but age is rejected from the Bacon age model; italic font: sample material is not suitable (pollen concentration <50%, dated material is affected by hard-water effect, or amount of datable carbon is too low) and age is rejected from the Bacon age model; na – information not available.

Sample ID	Core	Core segment	Segment depth (cm)	Tay 220 composite depth (cm)	Lab no.	^{14}C age BP (± 1σ)	C (mg)	Dated material	Calibrated age range (95.4%)	Calibrated median age BP (± 1σ)
AMS_20	**Tay 254**	**1-2**	**65-74.5**	**159**	**Poz-62344**	**4,345 ± 35**	**0.5**	**75% pollen**	**4,845-5,033**	**4,914 ± 47**
AMS_21	**Tay 254**	**1.5-2.5**	**3-12**	**168.25**	**Poz-62562**	**4,360 ± 40**	**na**	**80% pollen**	**4,849-5,039**	**4,927 ± 61**
AMS_22	Tay 254	1.5-2.5	12-22	178	Poz-62345	4,200 ± 40	0.5	85% pollen	4,588-4,849	4,730 ± 69
AMS_3	Tay 220	2-3	11-18	195	Poz-55862	5,010 ± 50	0.4	60% pollen	5,645-5,900	5,750 ± 77
AMS_23	**Tay 254**	**1.5-2.5**	**43-53**	**206.5**	**Poz-62553**	**4,780 ± 50**	**0.5**	**80% pollen**	**5,327-5,604**	**5,514 ± 71**
AMS_2	Tay 220	1.5-2.5	88-93	217.5	UGAMS-12598	4,240 ± 45	na	50% pollen	4,619-4,873	4,798 ± 75
AMS_4	*Tay 220*	*2-3*	*64-68*	*246*	*Poz-55866*	*4,360 ± 100*	*0.1*	*plant fibre fragment*	*4,651-5,306*	*4,976 ± 158*
AMS_30	**Tay 254**	**2-3**	**67-77**	**294**	**Poz-62556**	**5,240 ± 35**	**na**	**70% pollen**	**5,918-6,177**	**5,986 ± 70**
AMS_31	**Tay 254**	**2.5-3.5**	**9-18**	**313.5**	**Poz-62347**	**5,660 ± 30**	**na**	**70% pollen**	**6,324-6,503**	**6,440 ± 35**
AMS_43	Tay 254	2.5-3.5	19-25	322.75	Poz-79480	6,275± 35	0.6	60% pollen	7,030-7,275	7,212 ± 42
AMS_53	**Tay 220**	**2.5-3.5**	**58-63**	**334.5**	**Poz-87384**	**6,090 ± 40**	**0.5**	**70% pollen**	**6,803-7,156**	**6,957 ± 77**
AMS_44	Tay 254	2.5-3.5	29-36	335	Poz-79481	6,420± 35	0.8	85% pollen	7,278-7,422	7,357 ± 42
AMS_32	Tay 254	2.5-3.5	43-49	347.75	Poz-62557	5,430 ± 40	0.6	95% pollen	6,126-6,303	6,238 ± 45
AMS_1a	**Tay 220**	**3-4**	**2-5**	**349**	**UGAMS-12596**	**5,900 ± 55**	**na**	**55% pollen**	**6,567-6,883**	**6,723 ± 68**
AMS_1b	*Tay 220*	*3-4*	*2-5*	*349*	*UGAMS-12597*	*4,500 ± 40*	*na*	*70% charred plant particles*	*4,982-5,305*	*5,163 ± 84*
AMS_33	Tay 254	2.5-3.5	49-63	357.75	Poz-62559	5,435 ± 35	na	80% pollen	6,187-6,296	6,240 ± 35
AMS_5a	Tay 220	2.5-3.5	91-95	366.5	Poz-54258	5,440 ± 100	0.18	80% pollen	5,951-6,414	6,224 ± 118
AMS_34	**Tay 254**	**2.5-3.5**	**78-88**	**385.25**	**Poz-62560**	**6,000 ± 50**	**0.5**	**85% pollen**	**6,720-6,975**	**6,840 ± 66**
AMS_6	**Tay 220**	**3.5-4.5**	**0-9**	**412**	**Poz-55863**	**6,880 ± 40**	**0.4**	**80% pollen**	**7,620-7,818**	**7,712 ± 44**
AMS_7	**Tay 220**	**3.5-4.5**	**13-20**	**424**	**Poz-55864**	**7,080 ± 50**	**0.4**	**50% pollen**	**7,796-8,001**	**7,903 ± 49**
AMS_8a	**Tay 220**	**3.5-4.5**	**48-50**	**456.5**	**Poz-54259**	**7,100 ± 50**	**na**	**50% pollen**	**7,835-8,014**	**7,931 ± 49**
AMS_26	**Tay 254**	**3.5-4.5**	**24-34**	**459.5**	**Poz-62561**	**6,950 ± 50**	**0.8**	**70% pollen**	**7,680-7,925**	**7,780 ± 61**
AMS_40	*Tay 220*	*4-5*	*47-48*	*496*	*Poz62348*	*8,910 ± 70*	*0.3*	*mollusc*	*9,772-10,221*	*10,022 ± 122*
AMS_47a	*Tay 254*	*4-5*	*14.5-20.5*	*497.5*	*Poz-79041*	*9,110 ± 50*	*0.7*	*mollusc*	*10,408-10,195*	*10,263 ± 61*
AMS_47	**Tay 254**	**3.5-4.5**	**66.5-72**	**497.5**	**Poz-79427**	**7,450 ± 60**	**0.14**	**50% pollen**	**8,171-8,385**	**8,272 ± 62**
AMS_54	Tay 220	4.5-5.5	1-5	520.5	Poz-87385	6,670 ± 35	0.4	80% pollen	7,476-7,595	7,538 ± 31
AMS_50	Tay 254	4-5	38.5-45.5	521.25	Poz-79482	8,270 ± 50	na	50% pollen	9,091-9,430	9,265 ± 93
AMS_19	**Tay 220**	**4-5**	**87-90**	**537**	**Poz-55868**	**7,590 ± 40**	**na**	**50% pollen**	**8,341-8,453**	**8,395 ± 28**
AMS_14c	*Tay 220*	*5-6*	*0-4*	*559.5*	*Poz-55870*	*7,390 ± 60*	*0.2*	*60% charred plant particles*	*8,045-8,347*	*8,226 ± 80*
AMS_14p	**Tay 220**	**5-6**	**0-4**	**559.5**	**Poz-55869**	**7,660 ± 40**	**0.5**	**80% pollen**	**8,393-8,540**	**8,449 ± 42**
AMS_35	**Tay 254**	**4.5-5.5**	**44-54.5**	**566.5**	**Poz-62563**	**7,670 ± 70**	**0.4**	**80% pollen**	**8,375-8,591**	**8,470 ± 60**
AMS_16.1 NPP	*Tay 220*	*4.5-5.5*	*67-69*	*587*	*Poz-55871*	*8,440 ± 80*	*0.2*	*75% non-pollen palynomorphs*	*9,265-9,549*	*9,450 ± 82*
AMS_16.1 Ruppia	*Tay 220*	*4.5-5.5*	*67-69*	*587*	*Poz-55872*	*8,280 ± 50*	*0.7*	*6 Ruppia seeds*	*9,095-9,436*	*9,283 ± 92*
AMS_16.2	**Tay 220**	**4.5-5.5**	**67-69**	**587**	**Poz-55874**	**7,880 ± 70**	**0.2**	**80% pollen**	**8,549-8,981**	**8,716 ± 124**
AMS_36	**Tay 254**	**4.5-5.5**	**66-76**	**589.5**	**Poz-62564**	**7,940 ± 60**	**0.5**	**50% pollen**	**8,610-8,992**	**8,799 ± 110**
AMS_36c	*Tay 254*	*4.5-5.5*	*66-76*	*589.5*	*Poz-62566*	*8,330 ± 80*	*0.3*	*90% charred plant particles*	*9,500-9,092*	*9,333 ± 107*
AMS_17	*Tay 220*	*4.5-5.5*	*89-95*	*609*	*Poz-55875*	*7,410 ± 60*	*0.3*	*35% pollen, 35% tissues*	*8,050-8,374*	*8,247 ± 73*
S1-tephra*	**Tay 253**	**5-5.3**	**25-30**	**616**	**-/-**	**8,049 ± 49**	**na**	**terrestrial plant remains**	**8,725-9,090**	**8,939 ± 83**

* Modelled age of the S1-tephra as defined in the Dead Sea record[11].

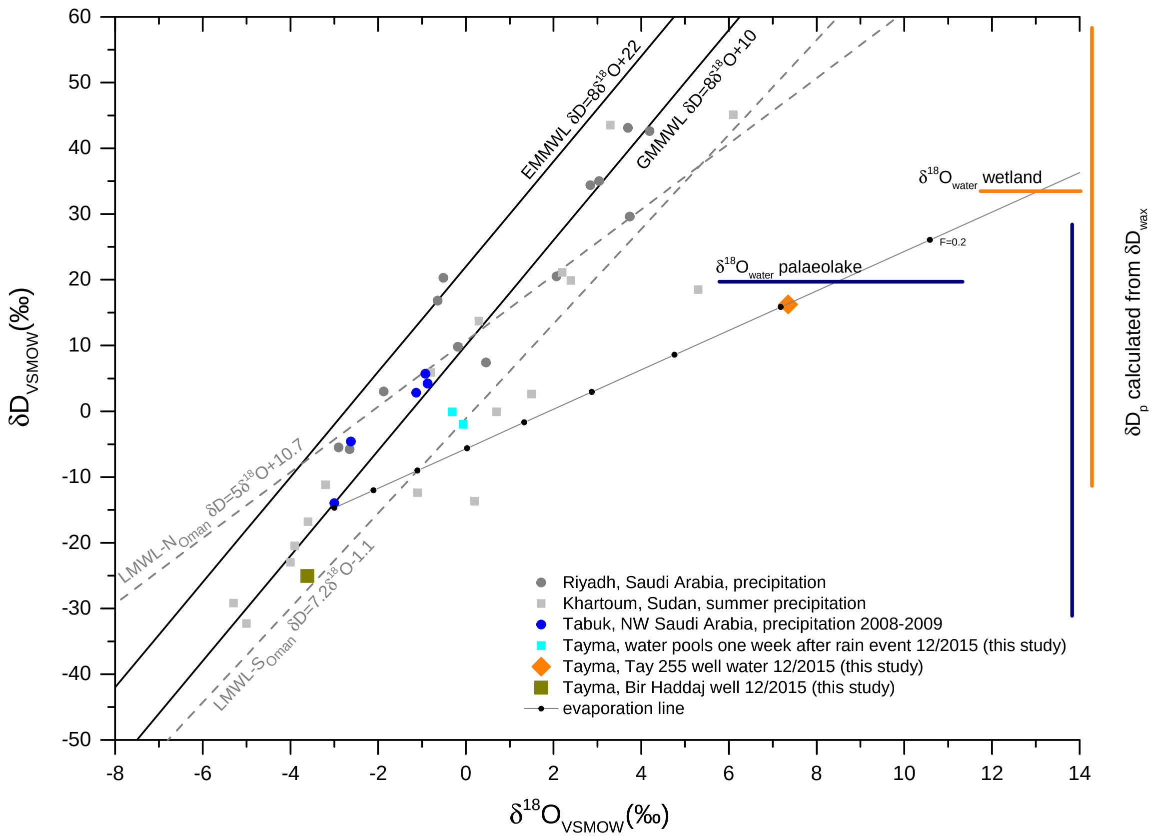

Supplementary Fig. 8: δD and δ^{18}O plot of Tayma palaeolake water and palaeo-moisture source reconstruction. For the isotopic characterisation of moisture sources, we used the Global Meteoric Water Line (GMWL) and Eastern Mediterranean Meteoric Water Line (EMMWL; high δD excess)[12], the two Local Meteoric Water Lines of rainstorm events in Oman[13], with LMWL-N (Mediterranean frontal systems; enriched δD) and LMWL-S (Indian Ocean cyclones and tropical depressions; depleted δD and δ^{18}O), the Red Sea-influenced rainstorm events in Riyadh[14] (partly enriched δD), the composition of the African monsoon precipitation (data from Khartoum, Sudan; partly depleted δD)[15], and few available precipitation data from Tabuk, NW Saudi Arabia[15], very close to Tayma. Surface rainwater collected in water pools in a wadi SW of the Tayma palaeolake show δ^{18}O values of around -0.5‰ and slightly enriched δD values. The stable isotopes of the Bir Haddaj well in Tayma reflect sub-surface groundwater with -3.5‰ δ^{18}O and -24.6‰ δD, similar to the middle of the Saq aquifer[16,17]. Groundwater sampled at 1.5 m depth in the well of Tay 255 (in 2015) shows highly enriched values of +7.4‰ $\delta^{18}O_{water}$ (+16.2‰ δD), only slightly lower than the calculated mean $\delta^{18}O_{water}$ of +8.4‰ for the palaeolake surface water between 8,800 and 7,950 cal yr BP. In comparison, the modelled mean $\delta^{18}O_{water}$ of the wetland phase between 7,800 and 6,800 cal yr BP is extremely heavy (+13.1‰). The difference between both settings will be mainly influenced by changes in precipitation and evaporation. Past precipitation estimates (δD_p) based on δD_{wax} range between -28 and +44‰ for the deep lake phase and -11 and +58‰ for the wetland phase, which may indicate a change in the predominant atmospheric moisture source. We calculated an evaporation line between $\delta^{18}O_{water}$ = -3‰ for the groundwater-supported lake and +7.4‰ of Tay 255 well water and found a high evaporation rate of >70% for the surface water of the deep lake and >80% for the shallow lake phase that reflect highly arid conditions.

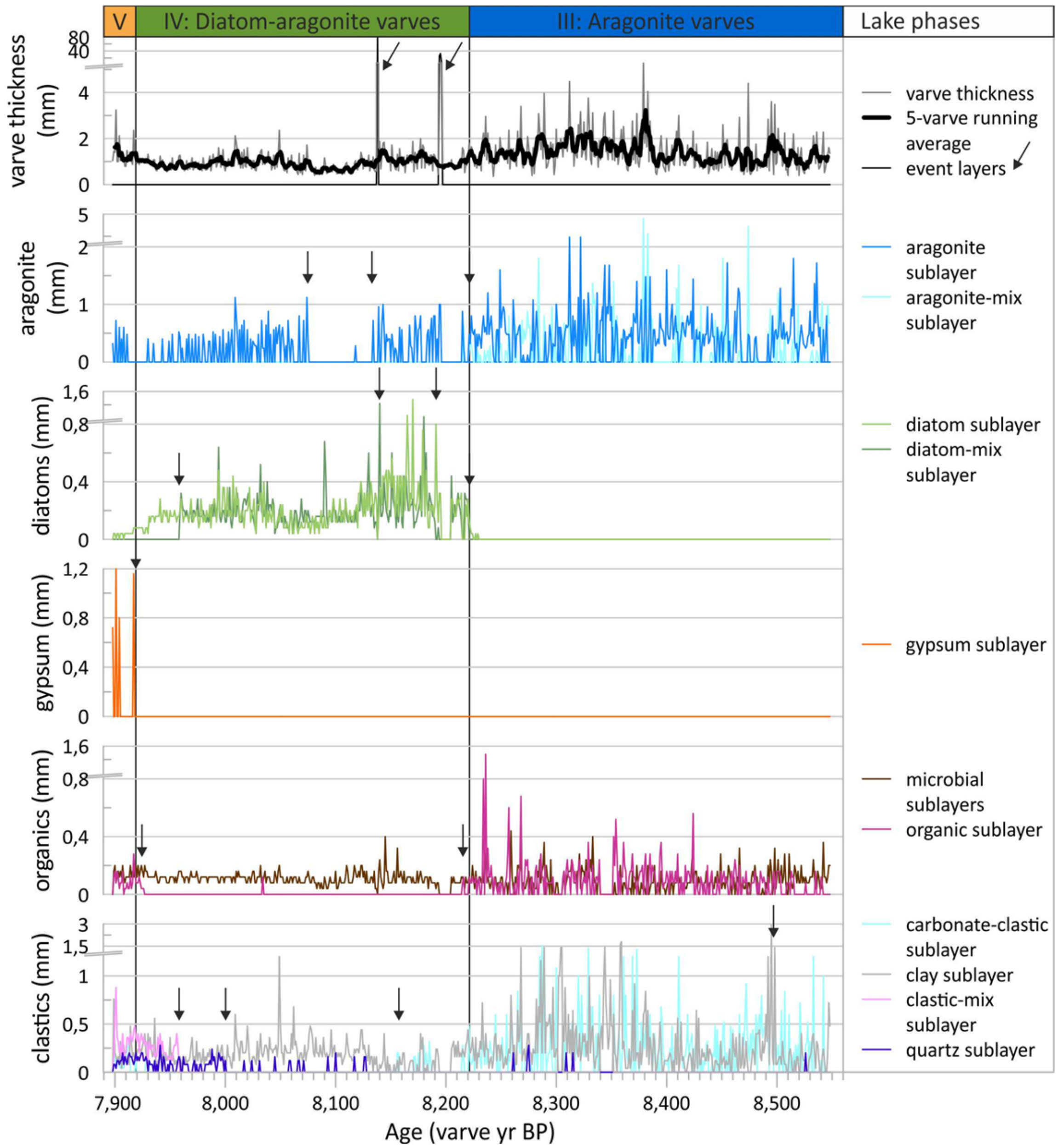

Supplementary Fig. 9: Varve micro-facies of lake phases III (aragonite varves), IV (diatom-aragonite varves) and V (transition to clastic-evaporitic lamination). Each varve (annual lamination) consists of at least two, but mostly three or more sublayers. Black arrows mark two several cm-thick graded event layers in the varve thickness panel (top); in the sublayer panels, arrows point either towards the onset or ceasing occurrence of a sublayer, or to particularly thick sublayers.

References

1. Engel, M. et al. The early Holocene humid period in NW Saudi Arabia – sediments, microfossils and palaeo-hydrological modelling. *Quat. Int.* **266**, 131–141 (2012).
2. Wellbrock, K. et al. in: *Taymāʾ I* (eds. Hausleiter, A., Eichmann, R. & al-Najem, M.) 145–198 (Archaeopress, 2018).
3. Al-Ahmadi, M. E. Hydrogeology of the Saq aquifer northwest of Tabuk, northern Saudi Arabia. *J. King Abdulaziz Univ. Earth Sci.* **20**, 51–66 (2009).
4. UN-ESCWA & BGR. *Inventory of shared water resources in Western Asia Ch 10* (Beirut, 2013).
5. Wellbrock, K., Strauss, M., Külls, C. & Grottker, M. in: *Des refuges aux oasis: Vivre en milieu aride de la Préhistoire à aujourd'hui. XXXVIIIe rencontres internationales d'archéologie et d'histoire d'Antibes* (eds. Purdue, L., Charbonnier, J. & Khalidi, L.) 231–249 (Éditions APDCA, 2018).
6. Vaslet, D. et al. *Geologic map of the Tayma quadrangle, sheet 27C: Kingdom of Saudi Arabia* (Ministry of Petroleum and Mineral Resources, 1994).
7. Engel, M. et al. Lakes or wetlands? A comment on 'The middle Holocene climatic records from Arabia: Reassessing lacustrine environments, shift of ITCZ in Arabian Sea, and impacts of the southwest Indian and African monsoons' by Enzel et al. *Global Planet. Change* **148**, 258–267 (2017).
8. Dinies, M., Neef, R., Plessen, B. & Kürschner, H. in *The Archaeology of North Arabia: Oases and Landscapes* (ed. Luciani, M.) 57–78 (Austrian Academy of Sciences Press, 2016).
9. Blaauw, M. & Christen, J. A. Flexible paleoclimate age-depth models using an autoregressive gamma process. *Bayesian Anal.* **6**, 457–474 (2011).
10. Reimer, P. J. et al. IntCal13 and Marine13 radiocarbon age calibration curves 0–50,000 Years cal BP. *Radiocarbon* **55**, 1869–1887 (2013).
11. Neugebauer, I. et al. Implications of S1 tephra findings in Dead Sea and Tayma palaeolake sediments for marine reservoir age estimation and palaeoclimate synchronisation. *Quat. Sci. Rev.* **170**, 269–275 (2017).
12. Gat, J. R. Oxygen and hydrogen isotopes in the hydrological cycle. *Annu. Rev. Earth Pl. Sc.* **24**, 225–262 (1996).
13. Weyhenmeyer, C. E., Burns, S. J., Waber, H. N., Macumber, P. G. & Matter, A. Isotope study of moisture sources, recharge areas, and groundwater flow paths within the eastern Batinah coastal plain, Sultanate of Oman. *Water Resour. Res.* **38**, 1184 (2002).
14. Michelsen, N. et al. Isotopic and chemical composition of precipitation in Riyadh, Saudi Arabia. *Chem. Geol.* **413**, 51–62 (2015).
15. IAEA & WMO. *Global Network of Isotopes in Precipitation. The GNIP Database.* https://nucleus.iaea.org/wiser (2018).
16. Alyamani, M. S. Isotopic composition of rainfall and ground-water recharge in the western province of Saudi Arabia. *J. Arid Environ.* **49**, 751–760 (2001).
17. Al-Sagaby, A. & Moallim, A. Isotopes based assessment of groundwater renewal and related anthropogenic effects in water scarce areas: Sand dunes study in Qasim area, Saudi Arabia. *IAEA-TECDOC* **1246**, 221–229 (2001).